CHAPTER 6

Singular Spectrum Analysis and Wavelet Analysis of Rainfall and Other Selected Meteorological Variables in NE India

Chapter 6

Singular Spectrum Analysis and Wavelet Analysis of Rainfall and Other Selected Meteorological variables in NE India

Contents

6.1 Introduction

Singular Spectrum Analysis (SSA)

The Singular Spectrum Analysis (SSA) is a well-developed technique in time series analysis [1], that provides knowledge of the dynamics of the underlying system that creates a time series, which are either unknown or only partially understood [2, 3]. It is recognized for its tremendous application areas- from mathematics, economics, to meteorology and oceanology [4-11]

SSA works at the basic two concepts. Here, the time series of interest is at first decomposed into various smaller components, and then the original series is reconstructed from the decomposed series. The forecasting of a time series can be achieved as well as, based on this decomposition-reconstruction technique. As SSA is a method based on window length, which decomposes a time series into various smaller components, therefore, the time series is not necessarily required to be linear or non-linear. Thus, this method is extremely helpful in analysing the climatic time series that are inherently in most cases, non-linear in nature [12].

The goal of SSA of a time series is the separability, i.e., to find out how well different components of a time series be separated from each-other. This leads to the use of SSA in the extraction and identification of trends of different resolution, seasonality components, extraction of inherent cycles and periodicities and in finding structure in short time series [6]. Vautard and Ghil [3] applied SSA in time series analysis of global surface air temperature, to isolate small numbers of inter-decadal (period of 21 and 16 years) and inter-annual (period of 6 and 5 years) oscillatory modes from the noise. In recent past, Marques et al. [9] performed successful application of SSA in extraction of trends from selected hydrological time series, i.e., annual rainfall, monthly runoff, and hourly water temperature over Portugal. Deng [4] also utilised SSA in extracting trend, seasonality, and residuals from monthly average sea temperature in a coastal region of South America and the outputs were then compared with other decomposition methods such as classical seasonal decomposition, seasonal decomposition by Loess (STL) and X-11. It was seen that the different components of the temperature series produced by the selected studied methods were non-identical but were highly correlated.

In the Indian context, recent findings depict the versatility of using SSA in the hydrological areas such as trend extraction in the hydrological time series and subsequent forecasting. Rangarajan [13] applied SSA in isolating the dominant principal components of homogeneous Indian Monsoon region rainfall series and its subsequent forecasting for the period 1871-1990. In this study, some inter-annual variability and a highly consistent phase was detected in the ranges of the annual variation in the three major principal components derived from SSA. However, it was concluded that the principal components were able to explain only slow and smooth changes in the signal and failed to explain the sharp and rapid fluctuations in the signals. Likewise, Unnikrishnan and Jothiprakash [14] applied SSA in extracting trend component of a daily rainfall time series for the Konya watershed, Maharashtra for the period 1961-2009. The SSA method was found to be successful in extracting non-linear trends from both the hydrologic time series. SSA was also applied in characterization of non-linear trends in rainfall time series by Aswathaiah and Nandagiri [15] for the period 1960-2015 for seventeen locations of India which were prone to irrigational activities since a decade ago. Keeping view of this, SSA was implemented to identify the possible change points in that region. The results of this study revealed existence of steep, nonlinear trends and distinctive break points in the direction of the trend.

Recent advancements show development of hybrid models using SSA based techniques in the field of hydrology. In such a scenario, Baratta et al. [16] applied an ensemble technique called as Quantitative Rainfall Forecasting (QRF) based on SSA to forecast daily time series of rainfall intensities at 135 stations in Tiber basin, Italy. The ensemble method combined an unsupervised decomposition followed by supervised learning. The average RMSE for the forecasted series was found to be <3. Another study by Alvarez-Meza et al. [10] described an automatic SSA based technique for the decomposition and subsequent reconstruction of daily averaged air temperature over Berlin, Germany for the period 2001-2004. The results revealed that the temperature time series could be decomposed into five different components. It was stated that the component with the highest power showed the cycle structure of the input time series, while the others might be related with the high frequency changes of the time series. This method was found to be successful in reconstruction of the original time series, discarding the noise elements. Pham et al. [17] developed a

Standardized Precipitation Index (SPI) drought forecasting model based on SSA and Single least square support vector machine (LSSVM). To develop the SPI index, nine-gauge stations and monthly areal rainfall data over Taiwan at monthly basis for a period of 41 years (1975-2015) were acquired. The drought forecasting models were developed in dual experiments: a) the LSSVM model with or without coupled with SSA and b) models with different inputs (antecedent SPIs and antecedent accumulated monthly rainfall) pre-processed by SSA. The findings of the study suggested that the accuracy of the SPI drought forecasting increased with b). In another study by Reddy et al. [18], SSA was coupled with two machine learning methods, i.e., least-squares support vector regression (LS-SVR), and Random-Forest (RF) to forecast rainfall over Nellore, Andhra Pradesh, India. They used 110 years of input data (Maximum, minimum and average temperature, vapour pressure, wind speed, relative humidity, and cloud cover) for the period 1901-2012 to predict monthly rainfall. It was revealed that the SSA technique could perform impressive forecasting of rainfall when combined with the machine learning based approaches.

Wavelet analysis

Wavelet technique is a powerful tool for decomposition of a time series into a scaled and shifted version of a particular wavelet. By definition, a wavelet is a mathematical function that may be used to divide a given function or continuous time signals into several frequency components and to analyse each one of them with a resolution corresponding to its scale. The oscillating waveforms of finite length/fast decay, known as the “mother wavelet” gives rise to the wavelets, which are the scaled and translated copies (called “daughter wavelet”) of their mother wavelet. The representation of a function by wavelets is known as a wavelet transform. They are considered as superior to the classical fourier transforms due to their ability of describing functions with strong peaks and discontinuities as well as for the precise deconstructing and rebuilding finite, non-periodic, and/or non-stationary signals [19]. Perfect reconstruction, i.e., the process of resembling a signal or image that has been divided into its component parts without losing any information, is a key characteristic of wavelet analysis. Because of these characteristics, wavelet methods have been considered as one of the potent and relevant methodologies in the areas of

signal processing and time series analysis and their widespread uses can be found in the hydro-meteorological studies [20].

Wavelet based approaches had been found to be carried out in decomposing various univariate time series (annual temperature of Central England, rainfall over the Everglades National Park, Florida and monthly NINO3.4 datasets) into its statistically significant components [21], detecting dominant periodicities responsible for the presence of trends in annual total precipitation over selected regions of Turkey [22], the variance and frequency-time localization as well with the detection of the dominant oscillations in rainfall as study of extremes [23], forecasting wind speed [24], investigating temporal variations in the dust storms over north China [25], studying Karst aquifers' (located in southern China) the response of discharge, suspended sediment and temperature to precipitation [26]. The findings of these studies indicate the promising performance of wavelet over other traditional linear models as well as wavelet as a coupled model with the modern advances of artificial intelligence.

Wavelet gained a worldwide popularity in the nineties. Wavelet transform was implemented in filtering and prediction of time series analysis since then by several researchers, such as Moghram and Saifur [27], Aussem et al. [28], and Khotanzad et al. [29]. Towards the late nineties numbers of research emerged based on different wavelet analyses of climatological series. Studies emphasizing the association of various indices of El Niño Southern Oscillation (ENSO) and other meteorological variables, mainly rainfall and sea surface temperature (SST) were extensively carried out using wavelet. Torrence and Compo [30] presented a step-by-step guide to time series analysis using wavelet on two climate indices of ENSO, viz. Niño3 sea surface temperature and Southern Oscillation Index (SOI). The results of this study revealed the variance of ENSO changing at an inter-decadal timescale, with a period of low variance during 1920-1960. The cross-wavelet power spectra revealed the changes in the Niño3 variance to be strongly associated with changes in the SOI. Likewise, Kestin et al. [31] applied wavelet along with windowed Fourier transform and windowed Prony's method to analyse time-frequency spectral structure of ENSO, where three indices, namely, SOI, Niño3 SST and a tropical Pacific rain index were analysed for variation in the spectral structures with time for the period 1871-1995. In

this study, large decadal changes could be noticed in the power distribution of SOI within 2-10 years periodicity band. In another study by Nakken [32], the temporal variability of rainfall and runoff and their inter-relationship over selected regions of central western New South Wales, Australia and association with SOI was investigated. The variability in rainfall, runoff and the relationship between them was found as changing over time; the association between SOI and rainfall over the region was found to be stronger after 1950s onwards, with a dominant frequency of SOI at 27 months. Similarly, Torrence and Webster [33] (1999) applied wavelet coherency on detection of inter-relationship between various ENSO and monsoon indices, where Nino3SST and Indian rainfall showed high coherence, especially during the intervals of high variance. Both of these parameters were found to be 180^{o} out-of-phase; with a gradual increase in phase difference Vs. Fourier period. Also, as detected in the wavelet power spectra, inter-decadal variations were observed in the indices in 2-7 years band, and intervals of high (1875-1920 and 1960-1990) and low (1920-1960) variance were also detected. Narasimha and Bhattacharyya [34] analysed the relation of ENSO with the solar activity and Indian monsoon rainfall for two test periods of 31 and 35 years (1878-1913 and 1933-1964) using wavelet cross-spectral analysis. An increased solar activity was found to be associated with a decrease in ENSO indices and an increase in monsoon rainfall in the 8-16 years period band. Within the period band of 2-7 years, the effects varied with the region. The findings from this study suggested that influence of solar processes on Indian monsoon rainfall functions in part indirectly through ENSO, but on more than one time scale.

In case of recent studies pertinent to India, literatures show the application of wavelet analyses related to precipitation. Subash et al. [35] applied Morelet wavelet for the detection of dominant periodicities prevailing in the total annual rainfall, rainfall during monsoon and during the months of June to September over five meteorological sub-divisions of central northeast India. In this study, periodic oscillations in the bands of 4-8 years and 30-34 years were observed for the western Uttar Pradesh (during September) and Bihar (during July) respectively. However, no significant periodicity was found to be associated with the rainfall over central northeast India as a whole. Determination of possible relationship of monthly precipitations and large-scale atmospheric circulation patterns with the application of wavelets had gained widespread observation. Rathinasamy et al. [36] applied wavelet in determining the

possible relationship of monthly rainfall extremes over thirty selected Indian regions with Nino3.4 and Indian Ocean Dipole (IOD). It was seen that significant inter-annual as well as inter-decadal oscillations (2-8 years and 8-32 years respectively) with variability in time and space were present in the extremes of monthly precipitation as detected by the wavelet spectra. Further on, these oscillations at the inter-annual and inter-decadal scales were found to be significantly driven by Nino3.4 and IOD in the wavelet coherence and partial wavelet coherence analysis. Likewise, in another research carried out by Das et al. [20] on monthly rainfall over six different locations of India for the period 1951-2015 with the help of global wavelet coherence, it could be seen that the Indian Summer Monsoon Index (ISMI) have the most effect on rainfall than the other selected indices IOD, SST, SOI, Multivariate ENSO Index (MEI), Pacific Decadal Oscillation (PDO), North Atlantic Oscillation (NAO) and Arctic Oscillation (AO). The phase difference between any of the climate indices and rainfall was non uniform in nature across India. However, rainfall was found to be in phase with ISMI in case of long terms of ISMI over all the studied locations of India. It was concluded that the wavelet and global coherence approach was a powerful tool in analyzing the association of multiple time series.

In the previous chapter (Chapter 5) the behaviour of precipitation along with other selected meteorological variables in terms of presence of inherent seasonal or cyclical components were discussed. Here, in this chapter we present the decomposition of monthly rainfall time series at the selected locations of NER (as discussed in Chapter 2), to segregate the different components consisting of the original rainfall series, and their individual contribution to the original time series using SSA. We've also incorporated wavelet analyses in this chapter, to analyse the rainfall time series in time-frequency space, to have an enhanced view of the detection and identification of oscillatory components constructing the rainfall time series over the region in a multiple-resolution way. Further on, the inter-relationships between rainfall and different meteorological variables, viz. temperature, relative humidity, sea level pressure and wind speed were examined using wavelet coherence and wavelet cross-spectrum. This chapter thus continues with the findings of the previous chapters and bridges the next chapter (chapter 7) that discusses the inter-relational sensitivity of the selected meteorological variables and rainfall over the NER

6.2 Basic Concepts

6.2.1 SSA

SSA is fundamentally a model-free technique; rather than being a confirmatory procedure, it is more of a tool for generating models. By not fitting an assumed model to the available series, it attempts to solve the issues of finite sample length and noisy sampled time series, yet, by utilising an adaptive data basis set. The description of the SSA approach in this chapter is in accordance with that given by Elsner and Tsonis [37]. and Golyandina et al [38].

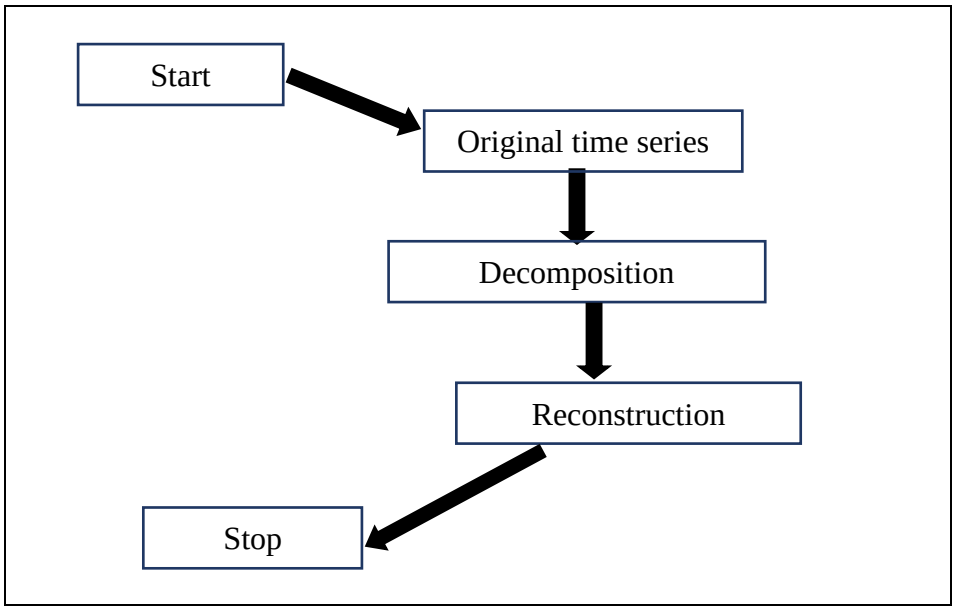

Figure 6. 1 Diagrammatic representation of the SSA analysis performed on the time series

There are three basic steps in SSA :

i) Embedding the sampled time series in a vector space of dimension M; then

ii) The M×M lag-covariance matrix $\mathbf{C_D}$ of the data is computed and finally

iii) $\mathbf{C_D}$ is diagonalized.

Embedding the sampled time series in a vector space of dimension M

The time series $x(t)$: $t=1, 2, ..., N$ is embedded into vector space of dimension M by considering M lagged copies $x(t-j)$: $j = 1, 2, ..., M$ of it. M is also known as 'window length'. The goal is to define the coordinates of the phase space that will roughly match the dynamics of the system from which the time record was collected by employing M lagged copies of a single time series [39, 40]. The number of lags is known as 'embedding dimension'. This method uses lagged (or delayed) copies of

segments of a time series, that is why the procedure is referred to as 'method of delays'.

Each lagged copy of a time series is used as a column vector, this is used for preparing trajectory matrix *X*. This way of constructing *X* is convenient to use the notation of an *(M, J)*-window, where M is the number of time series elements in each lagged copy (or embedding dimensions) and J is the sample times between each visible element. For SSA, *J=1* is used in which case it is only necessary to specify M and refer to the *(M,1)*-window as an *M*-window.

The selection of window length *M* is based on a compromise between information content and statistical confidence. Longer period oscillations, representing additional information above the strictly high frequency components, can be resolved with the larger window length. In contrast with the smaller window length, there is increase in statistical confidence because high frequency components do not compete with low frequency components for the limited available variance [41].

To resolve an oscillation of frequency f and a spectral bandwidth 2δ*f* using SSA, Vautard et al. [42] recommends.

$$\frac{1}{f} \leq M \leq \frac{1}{2\delta f}$$

As a good choice of M. These bounds cannot be determined a priori. Window length of M allows the distinction of oscillations with periods in the range of (*M/5, M*) suggested by empirical evidence [43].

The trajectory matrix **X** and its transpose $\mathbf{X^T}$ are the linear maps between the spaces R^M and R^N. The embedded space, R^M, is the space of all m-element patterns.

Computing the M×M lag-covariance matrix C_D of the data

There are many other ways to find lagged covariance matrix from a univariate time series. If we have a set of observations x_t, *t=1, 2, …., N*, Broomhead and King [2] proposed

$$(C_D)_{ij}^{(i)} = \frac{1}{N-M+1}\sum_{t=1}^{N-m+1} x_{i+t-1}x_{j+t-1}$$

Alternatively, suggested by Vautard and Ghil [3]

$$(C_D)_{ij}^{(2)} = \frac{1}{N-|i-j|}\sum_{t=1}^{N-|i-j|} x_{|i-j|+t}x_t$$

Here $(C_D)_{ij}^{(2)}$is a Toeplitz matrix, meaning that all the elements along each diagonal are the same.

Diagonalizing C_D

As C_D is symmetric and real, there exists a diagonalizing matrix **E** whose columns are orthonormal and a diagonal matrix Λ [44] such that

$$\mathbf{C_D = E\Lambda E^T}$$

$$\mathbf{C_D E = E\Lambda}$$

This is known as spectral decomposition of $\mathbf{C_D}$. Also ∧ is a diagonal matrix whose non-negative entries are the eigenvalues of $\mathbf{C_D}$. From the definition of $\mathbf{C_D}$, we have

$$\mathbf{X^T X E = E\Lambda,}$$

$$\mathbf{E^T X^T X E = \Lambda}$$

$$\mathbf{or\ (XE)^T (XE) = \Lambda}$$

trajectory matrix **XE** is the trajectory matrix projected onto the basis **E.** The components of **X** aligned along the basis **E** are uncorrelated as **E** is composed of orthogonal vectors $\mathbf{E_k}$ known as the singular vectors of **X**. The diagonal matrix **Λ** consisting ordered values $0 \leq \lambda_1 \leq \lambda_2 \leq \ldots\ldots \leq \lambda_M$ whose square roots are known as singular values that are referred to collectively as singular spectrum. These terms give SSA its name. Broomhead and King [2] showed method of obtaining the set $\{\lambda_k^{1/2}, E_k : 1 \leq k \leq M\}$ by singular value decomposition (SVD) applied to trajectory matrix **X.** $\mathbf{E_k}$**'s** are called the empirical orthogonal functions (EOF_s).

If there is arrangement of singular value in a plot is in decreasing order, one can often distinguish an initial steep slope, representing the signal, and a (more or less) "flat floor" represents the noise level [3].

It can be noted that the eigenvalues of $\mathbf{C_D}$ and the square roots of the eigenvalues of $\mathbf{C_D}$ are singular values, respectively, of **X.** In fact, **X** can be written as

$$\mathbf{X = DLE^T}$$

From the single value decomposition [44] (Press et.al.,1992), where **D** and **E** are left and right singular vectors of $\mathbf{X_t}$ and **L** is a diagonal matrix of singular values. Substituting for **X** in $\mathbf{C_D}$, we get

$$\mathbf{C_D = X^T X = (DLE^T)^T (DLE^T)}$$

$$\mathbf{=ELD^T DLE^T}$$

Since $\mathbf{D^T D=I}$, we have

$$\mathbf{S=EL^2E^T}$$

With the decomposition being unique to within a sign ambiguity, it follows that

$$\mathbf{L^2=\Lambda}$$

So, this is the right singular vectors of **X** that are eigenvectors of $\mathbf{C_D}$. Similarly, it can be shown that the left singular vectors of **X** are the eigenvectors of the matrix $\mathbf{XX^T}$.

Recovering the time series

The eigenvalues are used to compute the principal components (PCs) (a^k's) by projecting the original record on them as follows:

$$a_i^k = \sum_{j=1}^{M} x_{i+j-1} e_j^k, \qquad \text{for } i = 1, 2, \ldots, N,$$

Here e_j^k represents the j^{th} component of the k^{th} eigenvector. Each principal component a^k represents the projections of the original time series onto the k-th EOF. Sum of power spectra of PCs is identical to power spectrum of time series $x(t)$ [42]. Therefore, we can study separately the spectral contribution of various components. The PCs have length $N'=N-M+1$, not N, and do not contain phase information.

The recovery of any lost phase information during calculation can be done by reconstructing a signal from a convolution of one or more principal components with corresponding singular vectors which amount to

$$X_{i+j-1}=\sum_{k=1}^{M} a_i^k e_j^k$$

Where $i = 1, 2, ..., N$ and $j = 1, 2, ..., M$. The records can be filtered this way by using only a selection of possible principal components.

The pairs of high-variance eigenvalues $\lambda_k = \lambda_{k+1}$ are associated with oscillatory phenomena, observed by Vautard and Ghil [3]: both the corresponding PCs and EOFs are in quadrature (90^0 out of phase) with each other. The EOFs can be thought as data adaptive, anharmonic sine and cosine pair. This observation is true only for a pure oscillation but is found to hold in practice also for the paleoclimatic marine record [3]; the Vostok isotopic temperature record [45]; a record of 38 years mean monthly values of zonal wind at equator [46] and leading EOF analysis of geopotential heights taken daily at 700mb (Northern Hemisphere) and 500mb (Southern Hemisphere).

SSA, Noise and Signal Detection

The following assumptions in the eigenvalues decomposition is that the record has been taken from a process in which the stochastic component (noise) is a white noise process and is independent of signal bearing component (signal) of the process. In this way,

$$\mathbf{C_D} = \boldsymbol{C_D^{signal}} + \boldsymbol{C_D^{noise}}$$

If the process is corrupted by independent and identically distributed white noise, then

$$\boldsymbol{C_D^{noise}} = \boldsymbol{v^2 I}$$

$\mathbf{v^2}$ is noise variance, and **I** is identity matrix.

If we store the eigenvectors of $\mathbf{C_D}$ as columns in matrix **E**, then since C_D is symmetric

$$\mathbf{E^T C_D E} = \mathbf{E^T}(\boldsymbol{C_D^{signal}} + \boldsymbol{v^2 I})\ \mathbf{E} = \mathbf{\Lambda},$$

Where Λ is the diagonal matrix containing the eigenvalues of $\mathbf{C_D}$. with the eigenvectors forming an orthonormal basis we have

$$\mathbf{E^T I E} = \mathbf{I},$$

We can write

$$\mathbf{E^T}\boldsymbol{C_D^{signal}}\mathbf{E} = \mathbf{\Lambda} - \mathbf{v^2 I}.$$

Under the assumption of white noise, $\mathbf{C_D}$ AND $\boldsymbol{C_D^{signal}}$ share eigenvectors and their eigenvalues are related as follows:

$$\sum_{K=1}^{M} \boldsymbol{\lambda_K} = \sum_{K=1}^{M} \boldsymbol{\lambda_k^{signal}} + \boldsymbol{Mv^2}$$

6.2.2 Theory of Wavelet Analysis

The discrete wavelet transform (DWT), which functions similarly to the discrete fourier transform in spectrum analysis, is the fundamental tool required for examining time series using wavelets. The wavelet analysis methods described here follow Walker [47] and Percival and Walden's [48] approaches.

Let X be an N dimensional vector whose elements are real valued time series $\{X_t: t= 0,..., N-1\}$, where the sample size N is taken as integer multiple of 2^{j0} . Partial discreate wavelet Transform (DWT) of level J_o of X is an orthonormal transform given by $\mathbf{W}= WX$, where **W** is an N dimensional vector of DWT coefficients, and *W* is an N×N real valued matrix defining the DWT (if $N= 2^J$ and $J_0 = J$, we obtain a full DWT). The DWT coefficients **W** and matrix *W* can be partitioned such that

$$\mathbf{W} = \begin{bmatrix} \mathbf{W}_1 \\ \mathbf{W}_2 \\ . \\ . \\ . \\ . \\ . \\ \mathbf{W}_{Jo} \\ \mathbf{V}_{jo} \end{bmatrix} \quad \text{and } W = \begin{bmatrix} W_1 \\ W_2 \\ . \\ . \\ . \\ . \\ . \\ W_{Jo} \\ V_{jo} \end{bmatrix}$$

So that $\mathbf{W_j} = W_j X$ and $\mathbf{V_{jo}} = V_{jo}X$. Here $\mathbf{W_j}$ is an $N_j \equiv N/2^j$ dimensional vector of wavelet coefficients associated with change on scale $\tau_j \equiv 2^{j-I}$; W_j is an $N_j \times N$ dimensional matrix; $\mathbf{V_{jo}}$ is an N_{jo} dimensional vector of scaling coefficients associated with averages on scale $\lambda_{jo} \equiv 2^{Jo}$; and V_{Jo} is an $N_{Jo} \times N$ dimensional matrix.

The vector X can be synthesized from **W** via

$$X = W^T\mathbf{W} = \sum_{j=1}^{jo} W_j^T \mathbf{W_J} + V_{Jo}^T \mathbf{V_{Jo}} \equiv \sum_{j=1}^{jo} D_j + S_{Jo}$$

Which defines a multiresolution analysis (MRA) of X, i.e., an additive decomposition in terms of the N dimensional vectors $D_j = W_j^T \mathbf{W}_j$ (the jth level detail) and $S_{Jo} \equiv$

$V_{Jo}{}^{T}\mathbf{V_{Jo}}$ (J_oth level smooth), each of which can be associated with a particular scale (τ_j in case of D_j and λ_{Jo} in case of S_{Jo}).

In practice the DWT matrix *W* is not formed explicitly, but rather **W** is computed using a 'pyramid' algorithm that makes use of a wavelet filter and scaling filter and scaling filter. By definition, a filter $\{h_l : l = 0, \ldots, L-1\}$ of even width L (implying $h_o \neq 0$ and $h_{L-1} \neq 0$) is called a wavelet filter if,

$$\sum_{l=0}^{L-1} h_1 = 0 \text{ and } \sum_{l=0}^{L-1} h_1 h_{1+2n} = \begin{cases} 1, if & n = 0 \\ 0, if & n \; is \; a \; non-zero \; integer \end{cases}$$

Where the second summation expresses the orthonormality property of a wavelet filter (in the above $h_l \equiv 0$ for $l < 0 \; and \; 1 \geq L$, so we consider $\{h_l\}$ to be an infinite sequence with the most L nonzero values). The scaling filter is defined in terms of the wavelet filter via the 'quadrature mirror' relationship

$$gl \equiv (-1)^{l+1} h_{L-1-l}$$

The filter satisfies the conditions

$$\sum_{l=0}^{L-1} g_l g_{l+2n} = \begin{cases} 1, if \; n = 0; \\ 0, otherwise \end{cases} \text{ and } \sum_{l=0}^{L-1} g_l h_{l+2n} = 0 \text{ for all n.}$$

$\{h_l\}$ is normally a high-pass filter with a band pass given by $\frac{1}{4} \leq |f| \leq \frac{1}{2}$, while $\{g_l\}$ is nominally a low pass filter with pass band $0 \leq |f| \leq \frac{1}{4}$. Because each filter has a nominal pass band covering half and full band of frequencies, both $\{h_l\}$ and $\{g_l\}$ can be called half-band filters.

With $\{h_i\}$ and $\{g_i\}$ thus defined, the pyramid algorithm for stage j consists of circularly filtering the N_{j-1} elements of

$$\mathbf{V}_{j-1} \equiv [V_{j-1,0}, V_{j-1,1}, \ldots, V_{j-1,N_{j-1}-1}]^{T}$$

Retaining the filtered values with odd indices – this yields the j^{th} level wavelet and scaling coefficients, namely

$$\mathbf{W_{j,t}} \equiv \sum_{l=0}^{L-1} h_i V_{j-1,2t+1-i \bmod N_{j-1}}, \; \mathbf{V_{j,t}} \equiv \sum_{l=0}^{L-1} g_i V_{j-1,2t+1-i \bmod N_{j-1}},$$

Here,

t = 0, …., N_{j-1} (these are the elements of $\mathbf{W_j}$ and $\mathbf{V_j}$).

Given $\mathbf{W_j}$ and $\mathbf{V_j}$, the elements of $\mathbf{V_{j-1}}$ can be reconstructed (synthesized) via the j^{th} stage of the inverse pyramid algorithm, namely,

$V_{j-1,t} = \sum_{l=0}^{L-1} h_i V_{j-1,2t+1-i \bmod N_{j-1}} + \sum_{l=0}^{L-1} g_i V^{\uparrow}_{j,t+i \bmod N_{j-1}}$, t=0, 1, …, N_{j-1} -1,

Where,

$$W^{\uparrow}_{j,t} \equiv \begin{cases} 0, t = 0, 2, \dots, N_{j-1} - 2 \\ W_{j,\frac{t-1}{2}}, \ t = 1, 3, \dots, N_{j-1} - 1 \end{cases}$$

$V_j^{\uparrow},_t$ is defined similarly.

In this chapter, the monthly rainfall time series over selected study areas were subjected to SSA, with the aim to decompose them into their different components and the contribution of each of them in constructing the original time series was then computed. The monthly rainfall time series were simultaneously decomposed into different scales using discrete series of wavelet transform (DWT) ‘symlet8’ as the mother wavelet. Here the original time series was decomposed in nine levels or resolutions, yielding ten series w1 to w10 (depending upon the signal length l=588) at different scales. At each level of decomposition, a signal was decomposed into approximations (r_n; low frequency coefficients) and details (w_n; high frequency coefficients) using a low pass and high pass filters respectively [49]. A diagrammatic representation of the 9-level decomposition is depicted in Figure 6.2 (b). The individual wavelet spectra were analysed. The inter-relationship of rainfall with other selected meteorological variables (MaxT, MinT, RH, SLP and WS) was studied in the wavelet decomposed signals with the help of cross-wavelet transform and wavelet coherence. Wavelet coherence analyse the linkage between two time series within the time-frequency space by measuring the correlation between them [20]. The cross wavelet transform uncovers the common power and relative phase of two time series in time-frequency space, while the wavelet coherence reveals the significant coherence between two time series even when the common power is low [50]. The phase of the coherence spectra was also investigated. The wavelet decomposed 10

series were obtained for further used. These ten series were utilised in building a multi-resolution model with VAR-IRF. Figure 6.2 (a) and (b) depicts the thematic representation of the analysis thus performed.

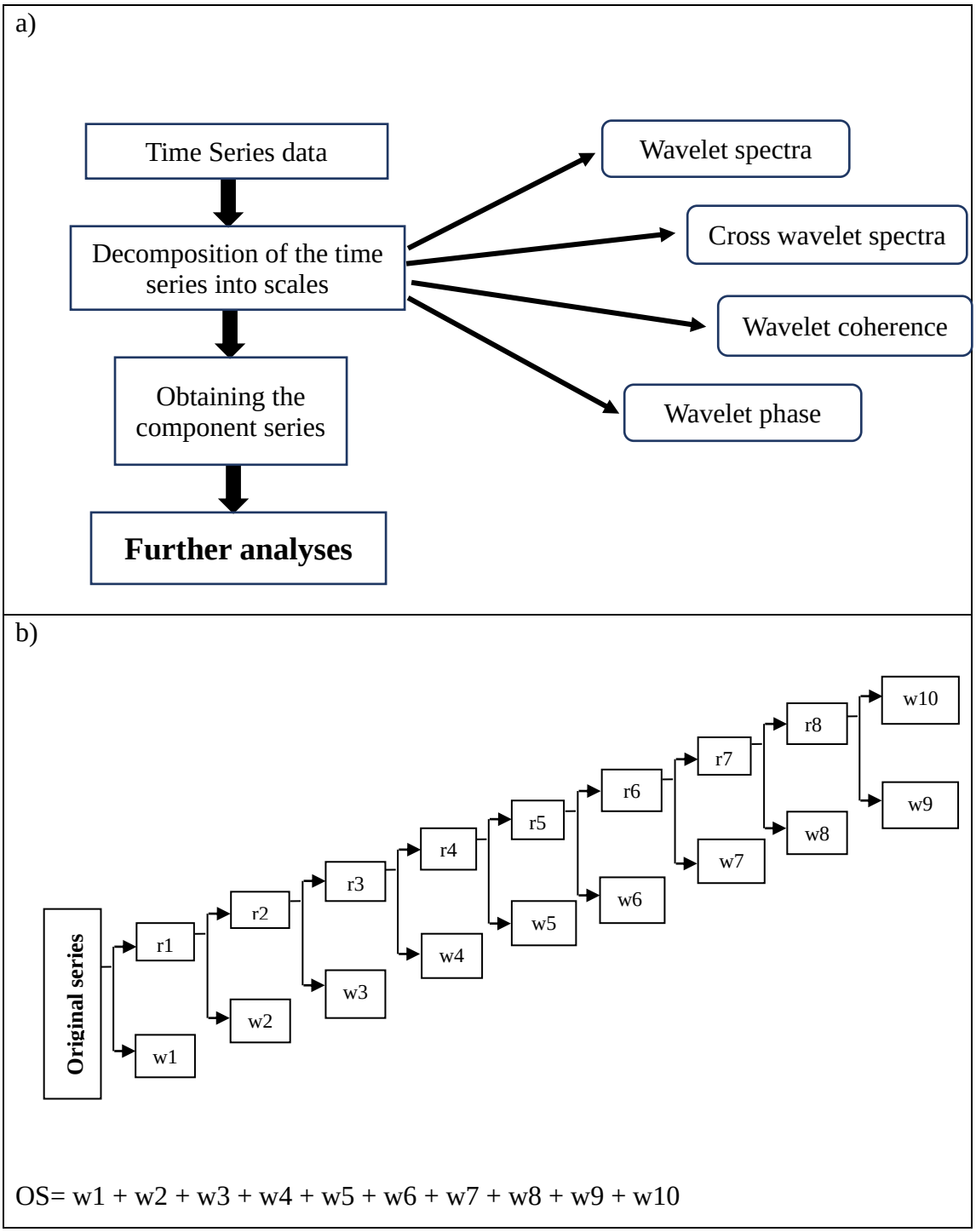

Figure 6. 2 a) Diagrammatic representation of the wavelet analysis performed on rainfall and the other selected meteorological variables; b) the 9-level wavelet decomposition resulting into ten series (w1-w10) of different resolutions (here l=588, so considering 2^n<l, decomposition levels are n= 9).

6.3 Results and discussion

6.3.1 SSA Analysis of rainfall

The results of SSA are described selected site wise in this section. The diagnostics of the computation for each site are elaborated with the help of the 1D plots of eigenvectors (a; Figures 6.3-6.7), the paired plots (2D scatterplots) for the first six eigenvectors pairs (b; Figures 6.3-6.7) and the screeplots of eigenvalues (c; Figures 6.3-6.7) of the decomposed rainfall series. The usefulness of these 1D and 2D graphs lies in the fact that the singular values of the two eigentriples (ET) of a harmonic series are often very close to each other, which makes the visual identification of the harmonic components easier. Also, an analysis of the scatterplots of the eigen vectors in a pairwise way allows clear visual identification of those eigentriples corresponding to the harmonic components of the series, provided those components are separable from the residual component [6]. The weighted (w-) correlation matrix for each original and reconstructed series was calculated, that can be explained with d; Figures 6.3-6.7. The w-correlation matrix is the matrix of weighted correlations between the elementary reconstructed components [5], that helps in checking for weak separability between the elementary components. The structure of each reconstructed component of the original series along with the residuals can be viewed in e; Figures 6.3-6.7.

As evident in Figure 6.3 (a), two slowly varying trend components (ET1 and ET6) were present in the deconstructed rainfall time series at CHR. Among them, ET1 contributed to a major percentage (42.06%) of the original series. The trend component ET6 seemed to be mixed with the signal, due to the appearance of seasonality within. Along with trend existed the periodic components that can be identified in the paired plots of the eigenvectors (Figure 6.3 b). The paired plot showed that the ET pairs 2-3 and 4-5 are produced by modulated sine waves, since the pure sine and cosine with equal frequencies, amplitudes, and phases create the scatterplot with the points lying on a circle, resembling regular polygons [51][6]. Thus, by counting the numbers of vertices in the paired plots the periods of the sine waves could be determined as 12 (ET 2-3) and 6 (ET 4-5). The contributions of these pairs were found to be the next highest (18.56+18.36% and 2.01+2% respectively). Thus, the 1st six components had a total of ~85% contribution to the original rainfall

series at CHR. The proportion of variance explained by each component constructing the original time series could be described with the help of the screeplot also (Figure 6.3 c). A significant drop in the eigenvalues was observed around component 6 in the x axis, beyond which could be considered as the residuals or noise. The weighted correlation between the ET pairs (up to ET10) were calculated and presented in the w-correlation matrix (Figure 6.3 d). Here, the matrix of absolute values of w-correlations was depicted in grayscale (the color from white to black corresponding to the absolute values of correlations from zero to one). It could be seen that the pairs ET2-3 and ET4-5 were separated between themselves as well as from the trend component (ET1). The final yield of the reconstruction could be seen in Figure 6.3 e, depicting clear view of the components (Trend, component1 and component2). In the reconstruction plots, the component 3 could be the manifestation of ET6, however the characteristics were not clearly identified.

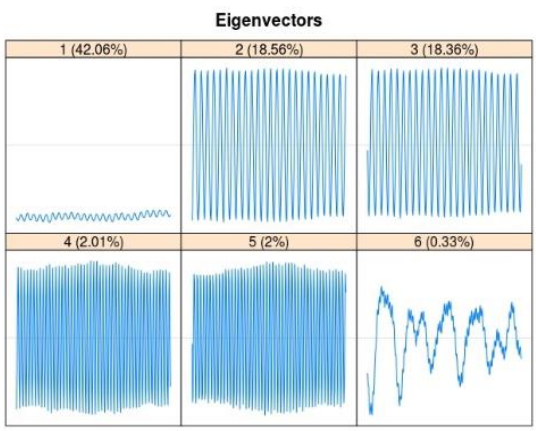

a)

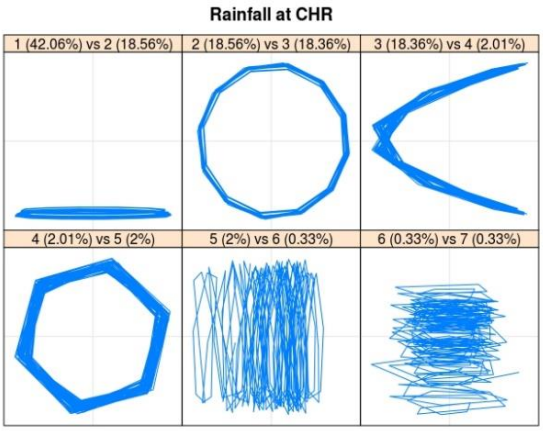

b)

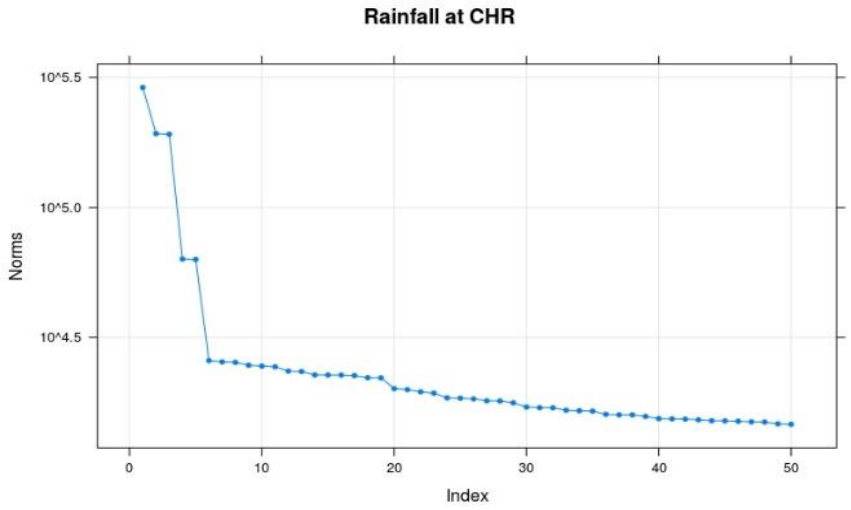

c)

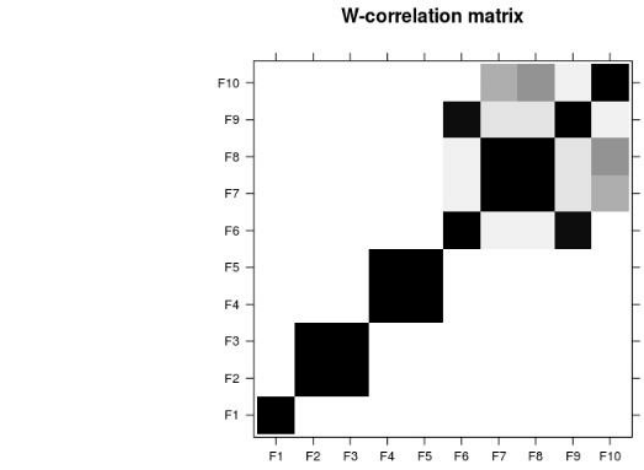

d)

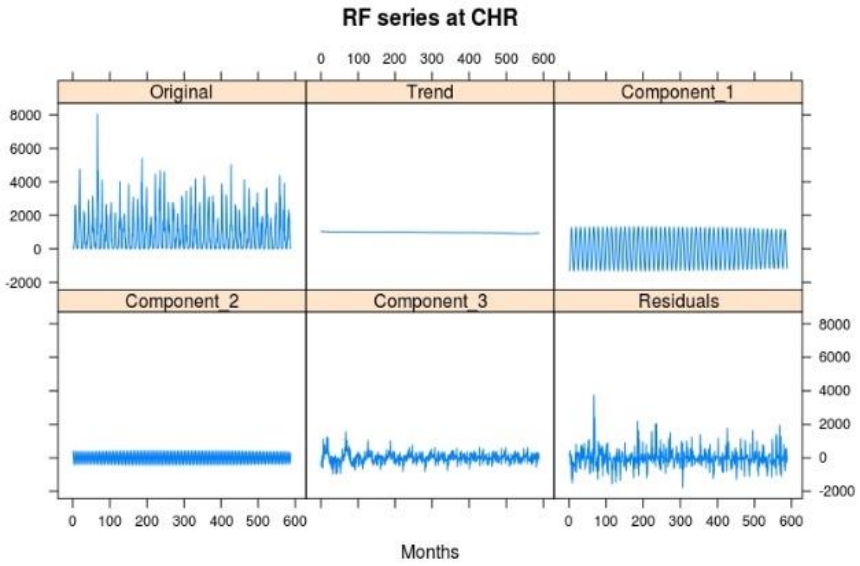

e)

Figure 6. 3 CHR: a) Eigen vectors for the 1st six components of the deconstructed monthly rainfall series, b) Paired plots for the 1st six eigen vectors of the decomposed series of rainfall, c) Screeplots of the eigenvalues in the decomposed rainfall series, d) W Correlation matrix for the original and reconstructed rainfall series and e) Reconstructed rainfall series (Original, Trend, Component 1, 2, 3 and Residuals); here the x axis denoted months

In case of monthly rainfall at DBR, the deconstruction resulted into a trend component (ET1) that contributed the highest (56.9%) among all as evident in Figure 6.4 a. The scatterplots of the eigenvector pairs (Figure 6.4 b) revealed that the components ET2-3 and ET4-5 were harmonic, with the periods of 12 and 6 respectively, similar to CHR. From both the 1D and 2D plots it was evident that these periodic components along with the trend component contributed ~88% to the original series. The w-correlation matrix supported the grouping of these paired components (Figure 6.4 d). The proportion of variance explained by each component constructing the original series can be seen in the screeplot (Figure 6.4 c), that

resembles similarity in structure with that in CHR. Finally, the outputs of reconstruction are presented in Figure 6.4 e, where the trend and the periodic components of 12- and 6-months present in the rainfall series were plotted. Similar to CHR, the component3 in this reconstructed plot could be the residuals as no information could be drawn from the plot.

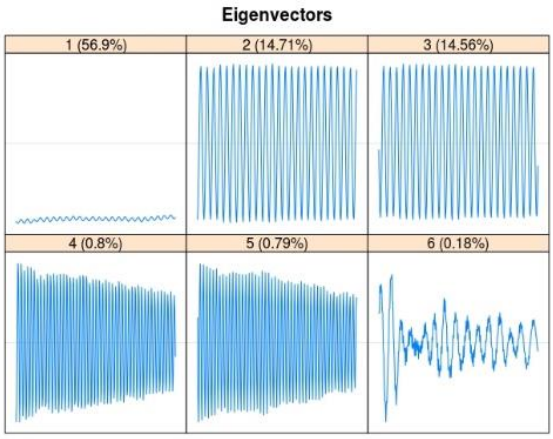

a)

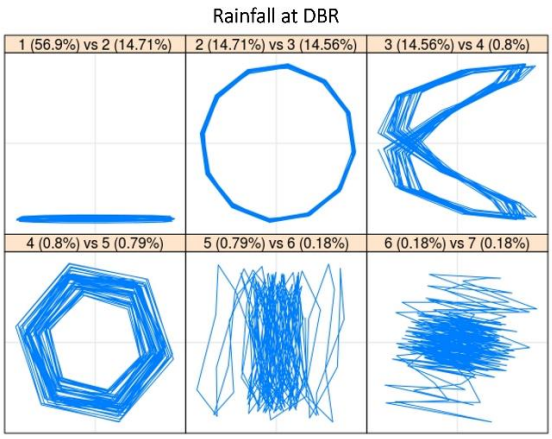

b)

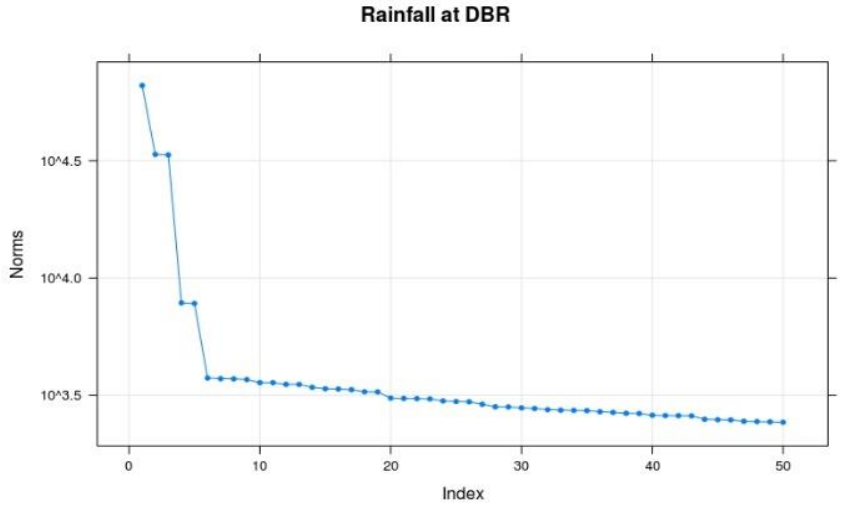

c)

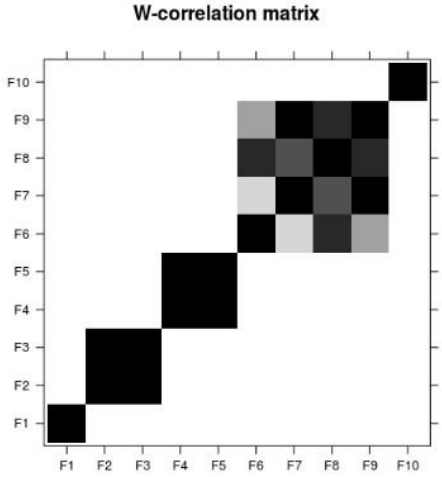

d)

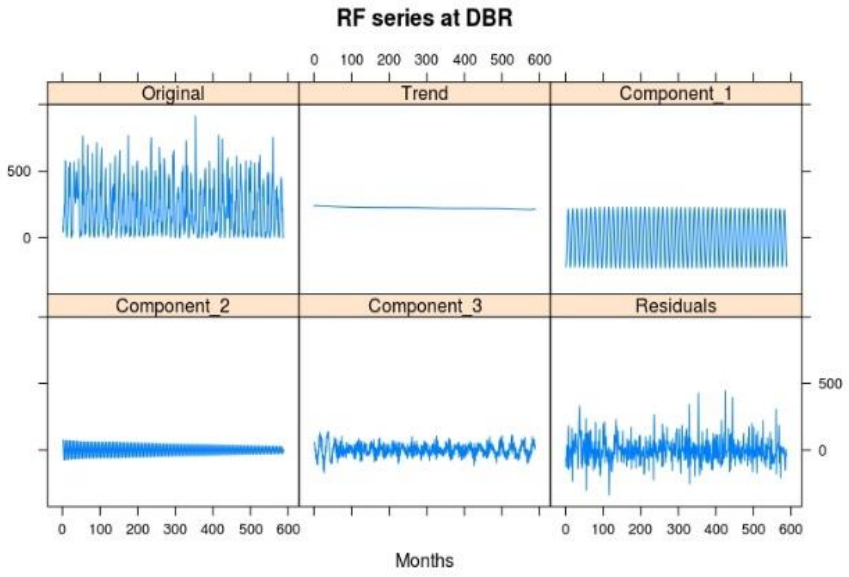

e)

Figure 6. 4 DBR: a) Eigen vectors for the 1st six components of the deconstructed monthly rainfall series, b) Paired plots for the 1st six eigen vectors of the decomposed series of rainfall, c) Screeplots of the eigenvalues in the decomposed rainfall series, d) W Correlation matrix for the original and reconstructed rainfall series and e) Reconstructed rainfall series (Original, Trend, Component 1, 2, 3 and Residuals); here the x axis denoted months

The deconstruction of monthly rainfall at GHY revealed the presence of trend components (ET1, 4 and 5), among which ET1was the highest contributor (52.85%), as evident in Figure 6.5a. However, like CHR, ET5 seemed to be mixed with the signal, due to the appearance of seasonality within. Two harmonic pairs of components ET2-3 and ET6-7, of periods 12 and 2.4 months respectively were identified along with the trend component behind the original rainfall series at GHY (Figure 6.5 b). However, the contribution of the ET6-7 to the original series was low (0.62%) as evident from the scatterplot. The screeplot (Figure 6.5 c) and the w-correlation matrix (Figure 6.5 d) identified the presence of other two pairs of components ET8-9, ET10-11, although the variance described by these pairs were minute (the F11 was not included while computing the w-correlation; hence the later pair was not detected clearly in the matrix). The reconstruction revealed the structure of the trends (depicted as trend and component 2 in Figure 6.5 e) and the periodic component 1 and 3 (corresponding to ET2-3 and ET6-7 respectively).

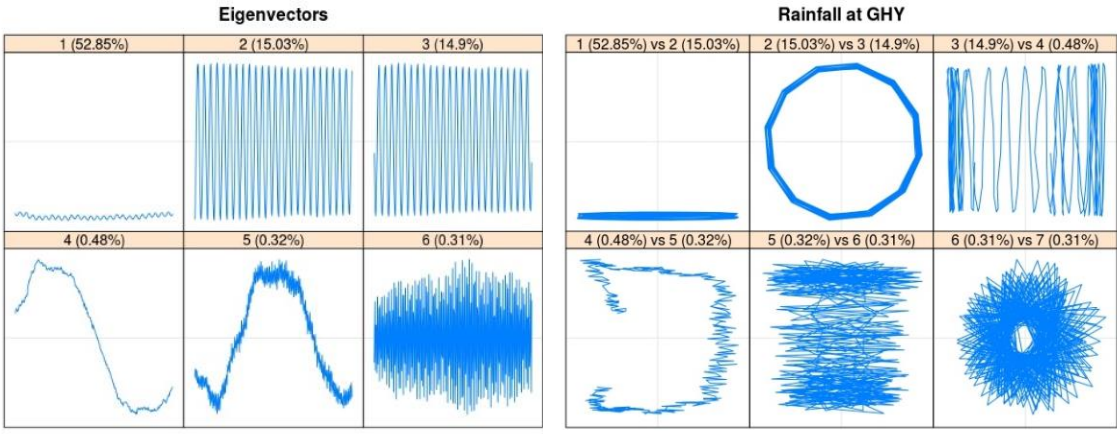
Eigenvectors
1 (52.85%)
2 (15.03%)
3 (14.9%)
4 (0.48%)
5 (0.32%)
6 (0.31%)
Rainfall at GHY
1 (52.85%) vs 2 (15.03%)
2 (15.03%) vs 3 (14.9%)
3 (14.9%) vs 4 (0.48%)
4 (0.48%) vs 5 (0.32%)
5 (0.32%) vs 6 (0.31%)
6 (0.31%) vs 7 (0.31%)

a) b)

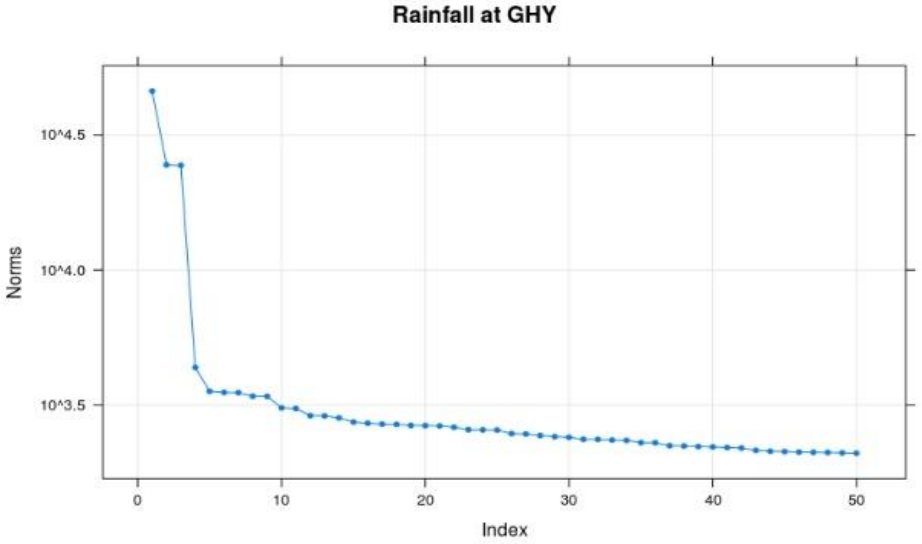
Rainfall at GHY
Norms
10^4.5
10^4.0
10^3.5
0
10
20
30
40
50
Index

c)

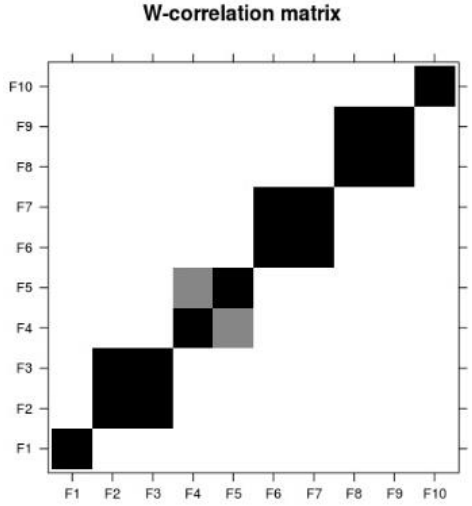
W-correlation matrix
F10
F9
F8
F7
F6
F5
F4
F3
F2
F1
F1
F2
F3
F4
F5
F6
F7
F8
F9
F10

d)

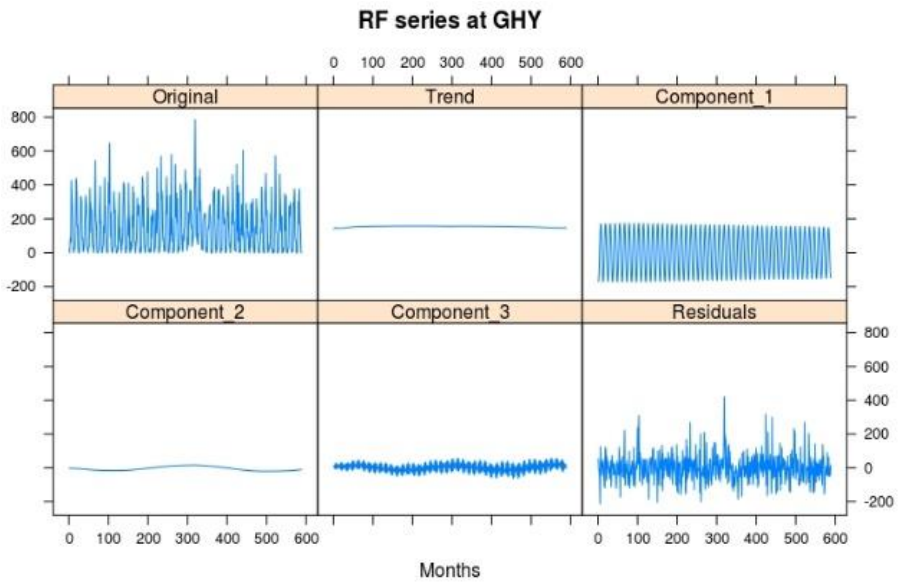

e)

Figure 6. 5 GHY: a) Eigen vectors for the 1st six components of the deconstructed monthly rainfall series, b) Paired plots for the 1st six eigen vectors of the decomposed series of rainfall, c) Screeplots of the eigenvalues in the decomposed rainfall series, d) W Correlation matrix for the original and reconstructed rainfall series and e) Reconstructed rainfall series (Original, Trend, Component 1, 2, 3 and Residuals); here the x axis denoted months

Similar to all the selected study sites, the deconstruction of monthly rainfall at KSH confirmed the presence of the trend component ET1 as the principle component of the original series, with a 56.10% contribution (Figure 6.6 a). Besides ET1, ET4 also revealed to be a trend component. The paired plots (Figure 6.6 b) identified two periodic components of 12 months and 4 months corresponding to the eigenvector pairs ET2-3 and ET5-6. The screeplot and the w-correlation matrix supported the grouping of the components. W-correlation matrix also grouped ET8-9. However, as the 1st six eigenvectors explained their largest cumulative contribution (~84%), ET8-9 was not characterised here. Structure of the final reconstruction plots of the trends and other components were similar to that in GHY.

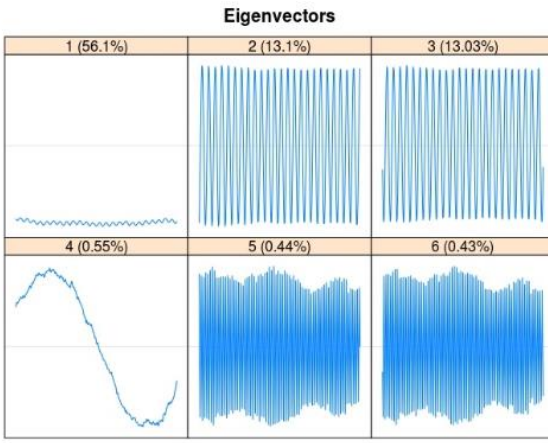
Eigenvectors
1 (56.1%)
2 (13.1%)
3 (13.03%)
4 (0.55%)
5 (0.44%)
6 (0.43%)

a)

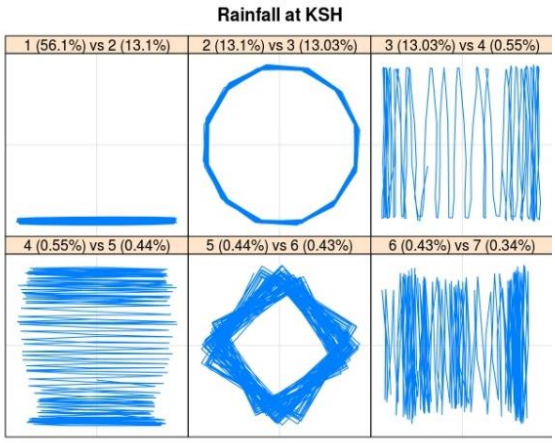
Rainfall at KSH
1 (56.1%) vs 2 (13.1%)
2 (13.1%) vs 3 (13.03%)
3 (13.03%) vs 4 (0.55%)
4 (0.55%) vs 5 (0.44%)
5 (0.44%) vs 6 (0.43%)
6 (0.43%) vs 7 (0.34%)

b)

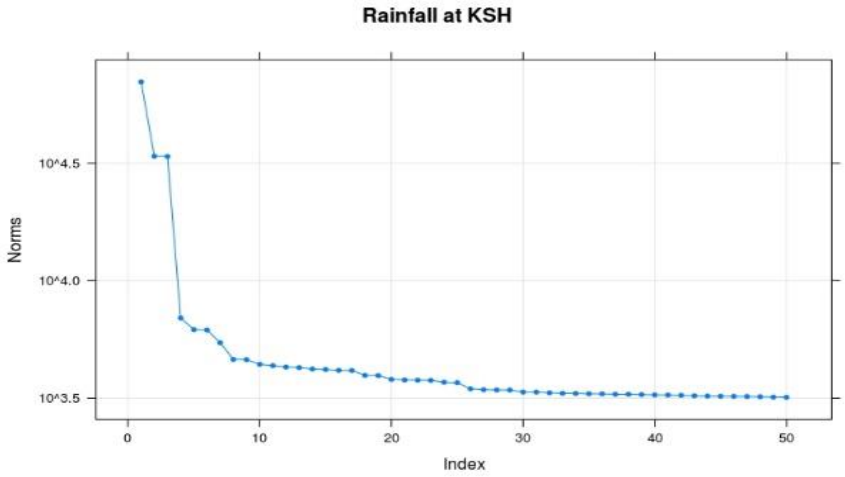
Rainfall at KSH
Norms
10^4.5
10^4.0
10^3.5
0
10
20
30
40
50
Index

c)

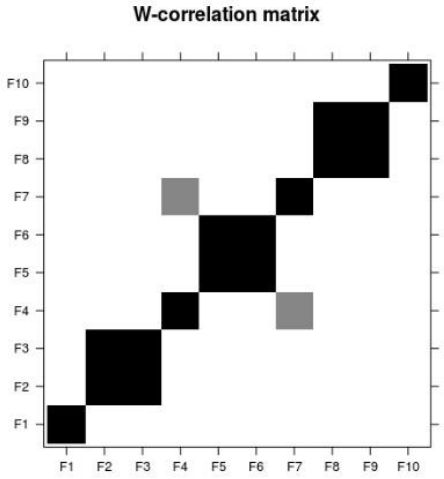
W-correlation matrix
F10
F9
F8
F7
F6
F5
F4
F3
F2
F1
F1
F2
F3
F4
F5
F6
F7
F8
F9
F10

d)

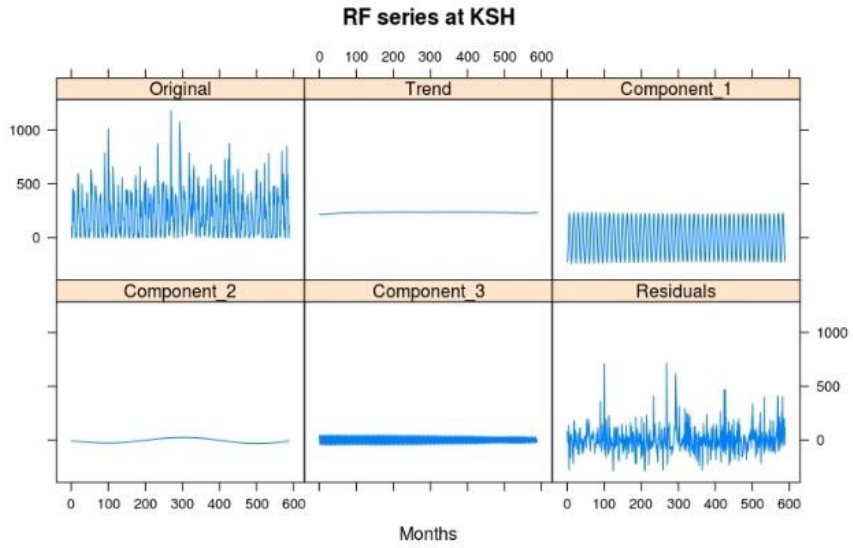

e)

Figure 6. 6 KSH: a) Eigen vectors for the 1st six components of the deconstructed monthly rainfall series, b) Paired plots for the 1st six eigen vectors of the decomposed series of rainfall, c) Screeplots of the eigenvalues in the decomposed rainfall series, d) W Correlation matrix for the original and reconstructed rainfall series and e) Reconstructed rainfall series (Original, Trend, Component 1, 2, 3 and Residuals); here the x axis denoted months

At TUL three trend components (ET1, 4 and 5) could be identified from the eigenvectors plots (Figure 6.7 a). The paired plots identified ET2-3 as the harmonic components with 12 months period. From the w-correlation matrix (Figure 6.7 d) the grouping of ET4 and 5 suggested that they might be of similar forms. W-correlation matrix also grouped ET8 and 9, but from the screeplot (Figure 6.7 c) however, component6 (ET6) seemed to be starting of the noisy floor as was evident in CHR. Thus, the contribution of ET8-9 was not depicted here, considering very low. The reconstructed series could be seen in Figure 6.7 e, with the detected periodic component (as component 1 in the figure) and the trend components (as trend and component 2 in the figure). The reconstruction plots revealed ET4 and 5 to be of similar form, as component 3 in the figure.

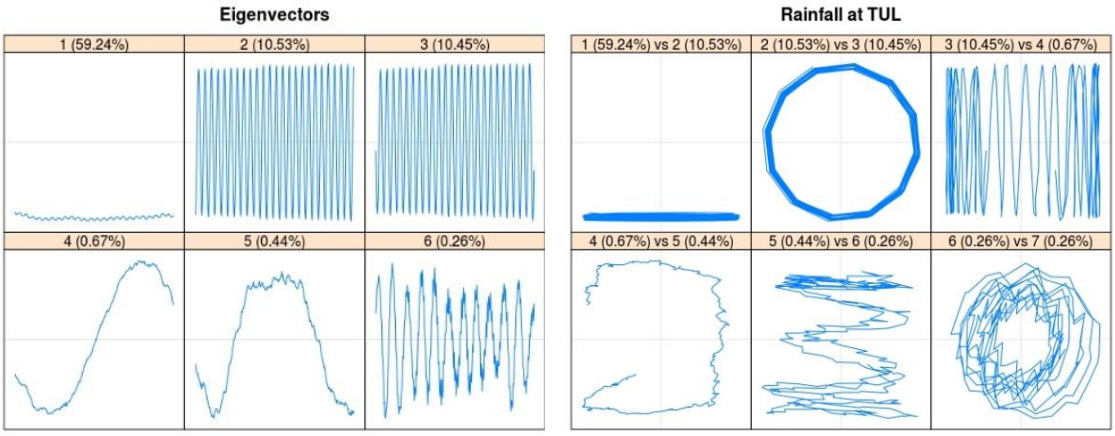
Eigenvectors
1 (59.24%)
2 (10.53%)
3 (10.45%)
4 (0.67%)
5 (0.44%)
6 (0.26%)
Rainfall at TUL
1 (59.24%) vs 2 (10.53%)
2 (10.53%) vs 3 (10.45%)
3 (10.45%) vs 4 (0.67%)
4 (0.67%) vs 5 (0.44%)
5 (0.44%) vs 6 (0.26%)
6 (0.26%) vs 7 (0.26%)

a) b)

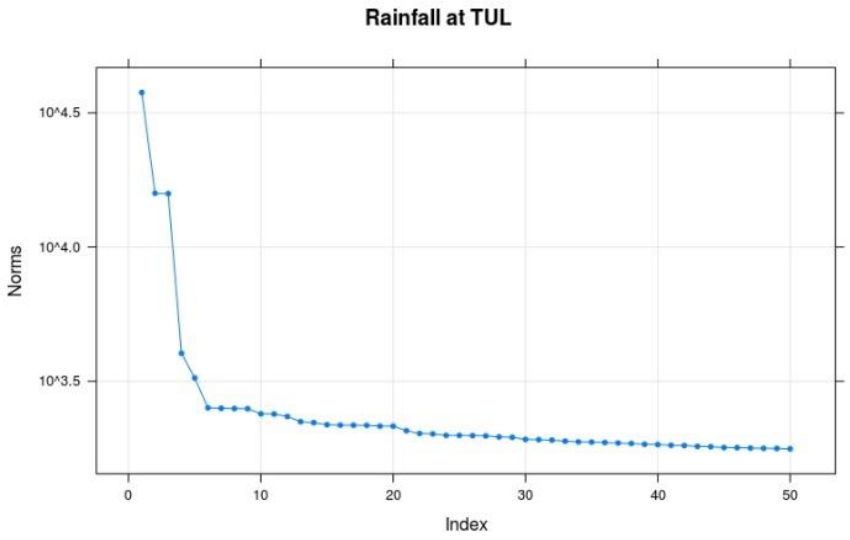
Rainfall at TUL
Norms
10^4.5
10^4.0
10^3.5
0
10
20
30
40
50
Index

c)

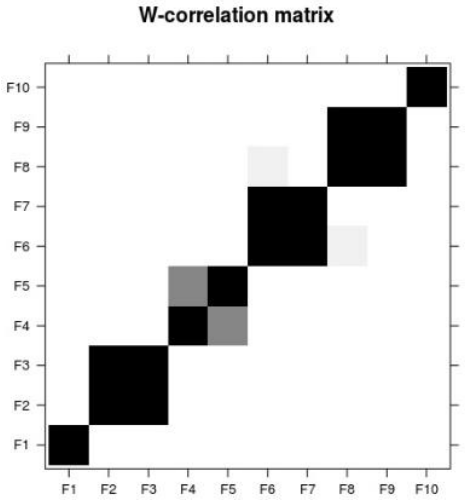
W-correlation matrix
F10
F9
F8
F7
F6
F5
F4
F3
F2
F1
F1
F2
F3
F4
F5
F6
F7
F8
F9
F10

d)

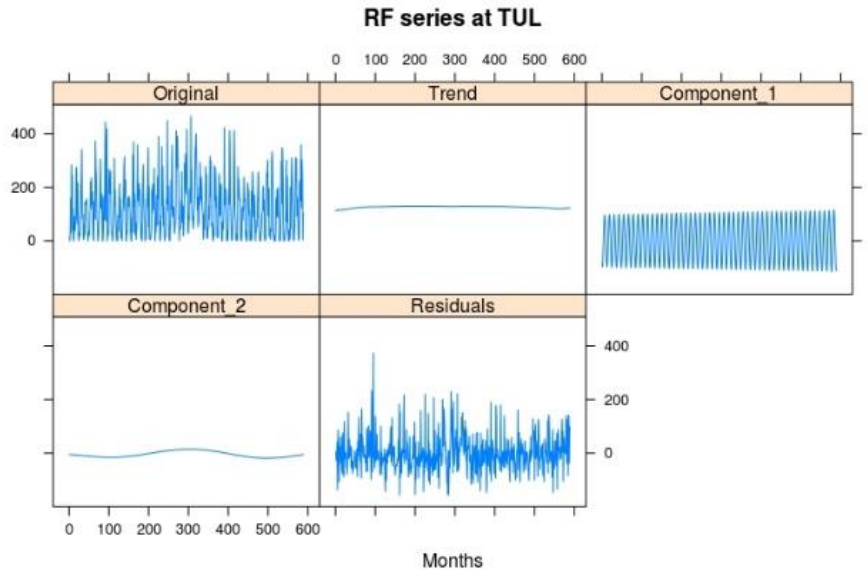

e)

Figure 6. 7 TUL: a) Eigen vectors for the 1st six components of the deconstructed monthly rainfall series, b) Paired plots for the 1st six eigen vectors of the decomposed series of rainfall, c) Screeplots of the eigenvalues in the decomposed rainfall series, d) W Correlation matrix for the original and reconstructed rainfall series and e) Reconstructed rainfall series (Original, Trend, Component 1, 2, 3 and Residuals); here the x axis denoted months

6.3.2 Wavelet Analysis of monthly rainfall

Wavelet power spectrum

As evident in the Figure 6.8 (a-e), the rainfall time series at all studied sites displayed significant (1% significance level, showed within white colored contour) high power (as designated by the wavelet power levels in the right) in the 8–16 month-band in the period throughout the 588 months (1969-2017). In this band, the one-year period (i.e., 12 months) was of the highest wavelet power (Figure 6.8 a-e, black coloured ridge). The one-year period of high power could be attributed to the monsoonal influence of rainfall in this reason. High frequency oscillations were also prominent in the 2-8 months band in the period, per every 10 months during 1969-2017, in the rainfall time series at all selected locations of NER. In case of KSH and TUL, significant high powers were detected in the 16-32 months band in around the 280^{th}-320^{th} month (1992-1996). The strength of this high power was greater in TUL than in KSH.

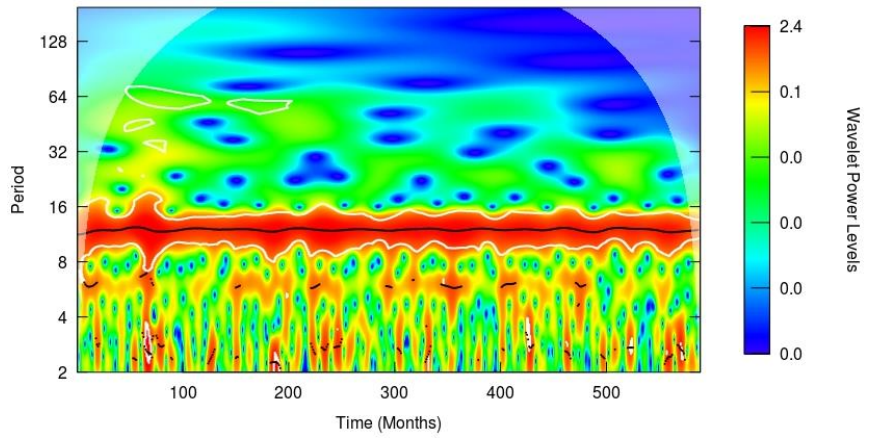
Period
128
64
32
16
8
4
2
100
200
300
400
500
Time (Months)
2.4
0.1
0.0
0.0
0.0
0.0
Wavelet Power Levels

a)

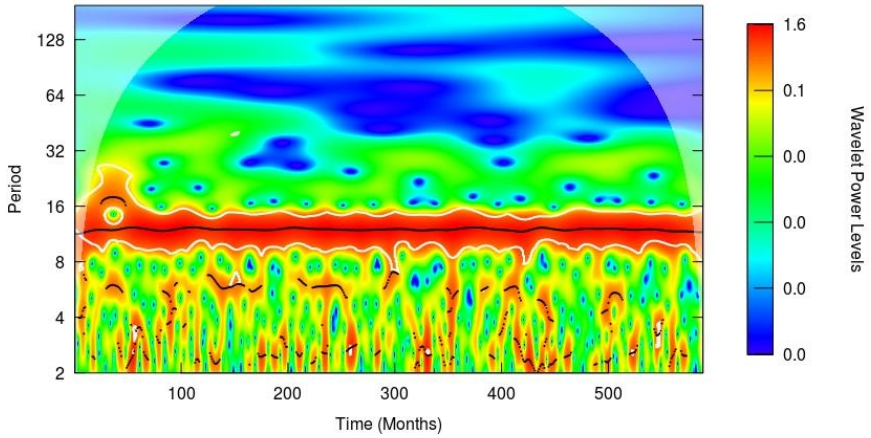
Period
128
64
32
16
8
4
2
100
200
300
400
500
Time (Months)
1.6
0.1
0.0
0.0
0.0
0.0
Wavelet Power Levels

b)

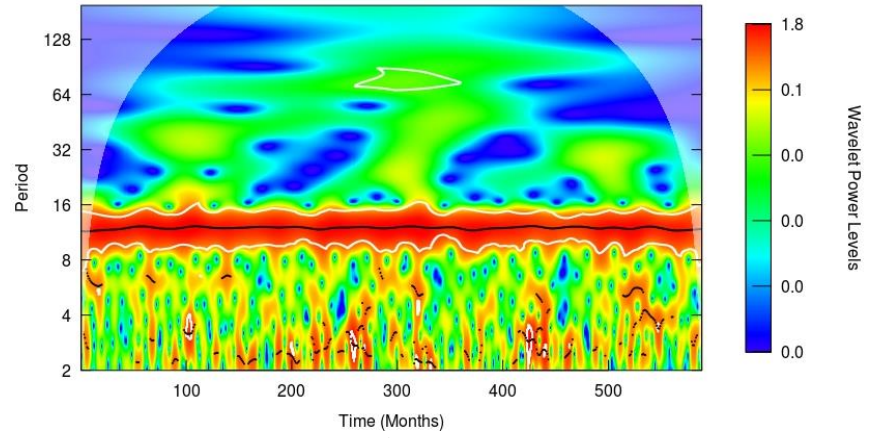
Period
128
64
32
16
8
4
2
100
200
300
400
500
Time (Months)
1.8
0.1
0.0
0.0
0.0
0.0
Wavelet Power Levels

c)

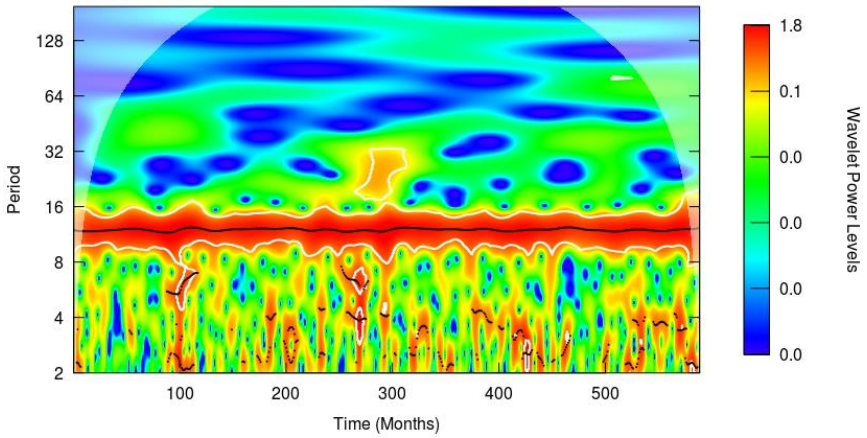

d)

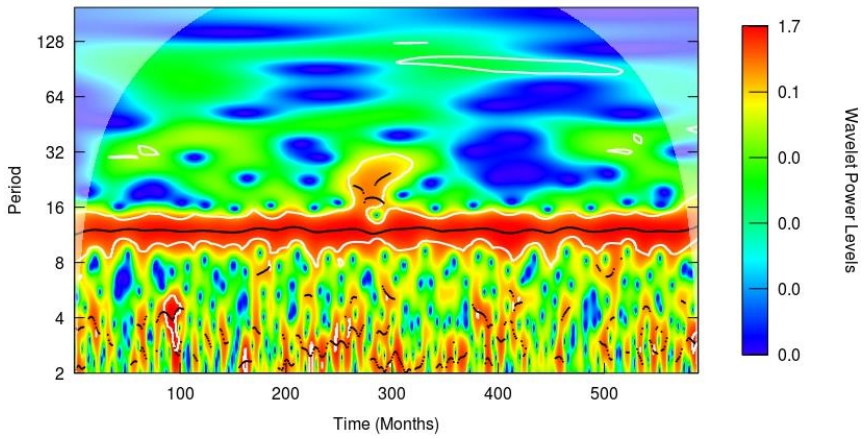

e)

Figure 6. 8Wavelet power spectrum of rainfall at a) CHR, b) DBR, c) GHY, d) KSH, e) TUL of NER. The cone of influence is designed as a lighted shadow; here the Y axis indicates Fourier period in months.

Cross-wavelet transform, and Wavelet coherence transform

The results of cross-wavelet transform, and wavelet coherence transform applied on the time series of meteorological variables can be elaborated with the help of the cross-wavelet spectrum (XWT) plot and wavelet coherence transform (WCT) plot for each association. The sign conventions for understanding a cross-wavelet and wavelet coherence plot are as follows:

In phase association is indicated by " → " (Horizontal arrows pointing to right)

Anti-phase association is indicated by " ← " (Horizontal arrows pointing to left)

When the 1st variable (rainfall) is leading " ↘ " or " ↖ "

When the 2nd variable (the other one) is leading " ↗ " or " ↙ "

Rainfall with MaxT

As evident from the XWT plots (Figure 6.10 a-e), significant strong common power was present in the period band of 8-16 months for rainfall and MaxT, continuous throughout the study period across all the selected regions of NER. It was also evident that these parameters were in-phase with significant common power. Significant strong intermittent powers in anti-phase could be found in the period band of 4-8 months in the cross-wavelet spectrum at CHR, GHY and KSH around the 270th-280th month (1991-1992), but the power was relatively weaker than that in the 8-12 months period band. The WCT plots (Figure 6.10 a-e) also revealed the features that were detected in the XWT plots. Additionally, it detected strong significant associations between rainfall and MaxT even in the regions of low common powers of the XWT, e.g., strong significant associations could be seen in the low frequency bands (period band of 64-128) at DBR (starting from the 340th month, i.e., the year 1997), CHR and the other locations (localised patches) in the WCT plots. All of these associations were anti-phase in nature. The WCT plots at CHR, DBR and KSH exhibited much localized significant common powers at the frequency band 32-64. Inter-decadal coherence was present at CHR in the high frequency band of 4-8 months, and this coherence were anti-phase, most prominent in between the 300th-500th months duration (1994-2010).

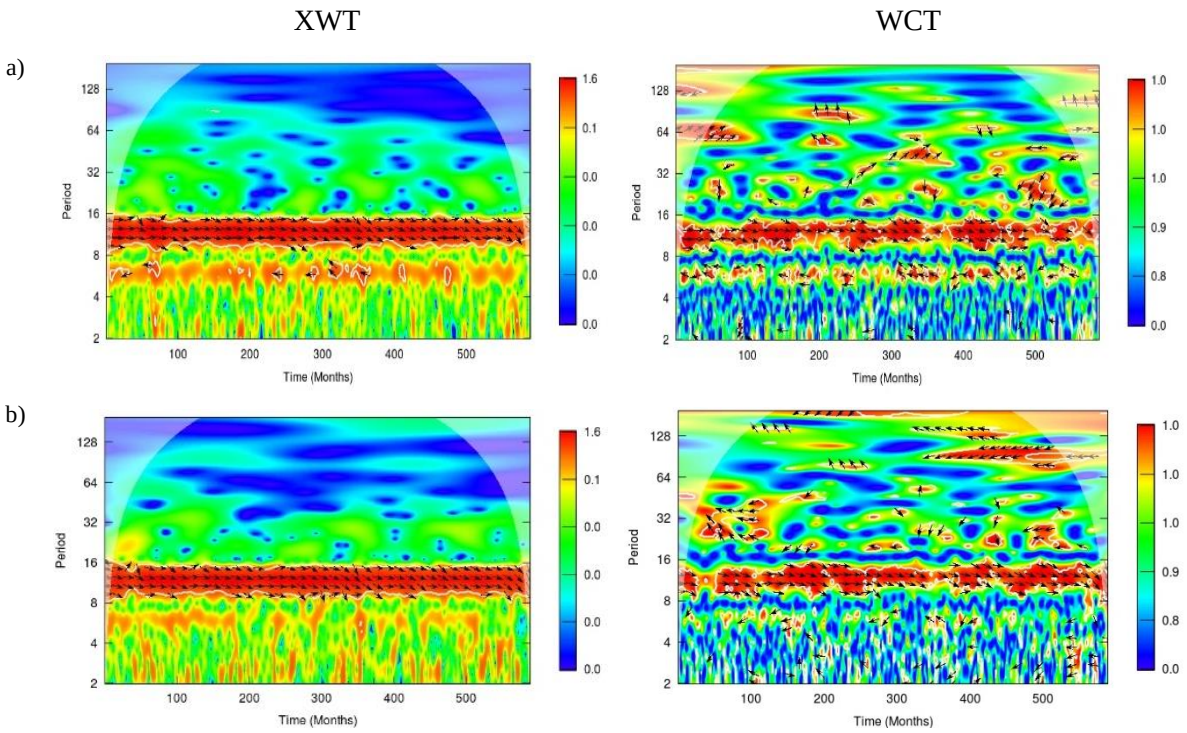

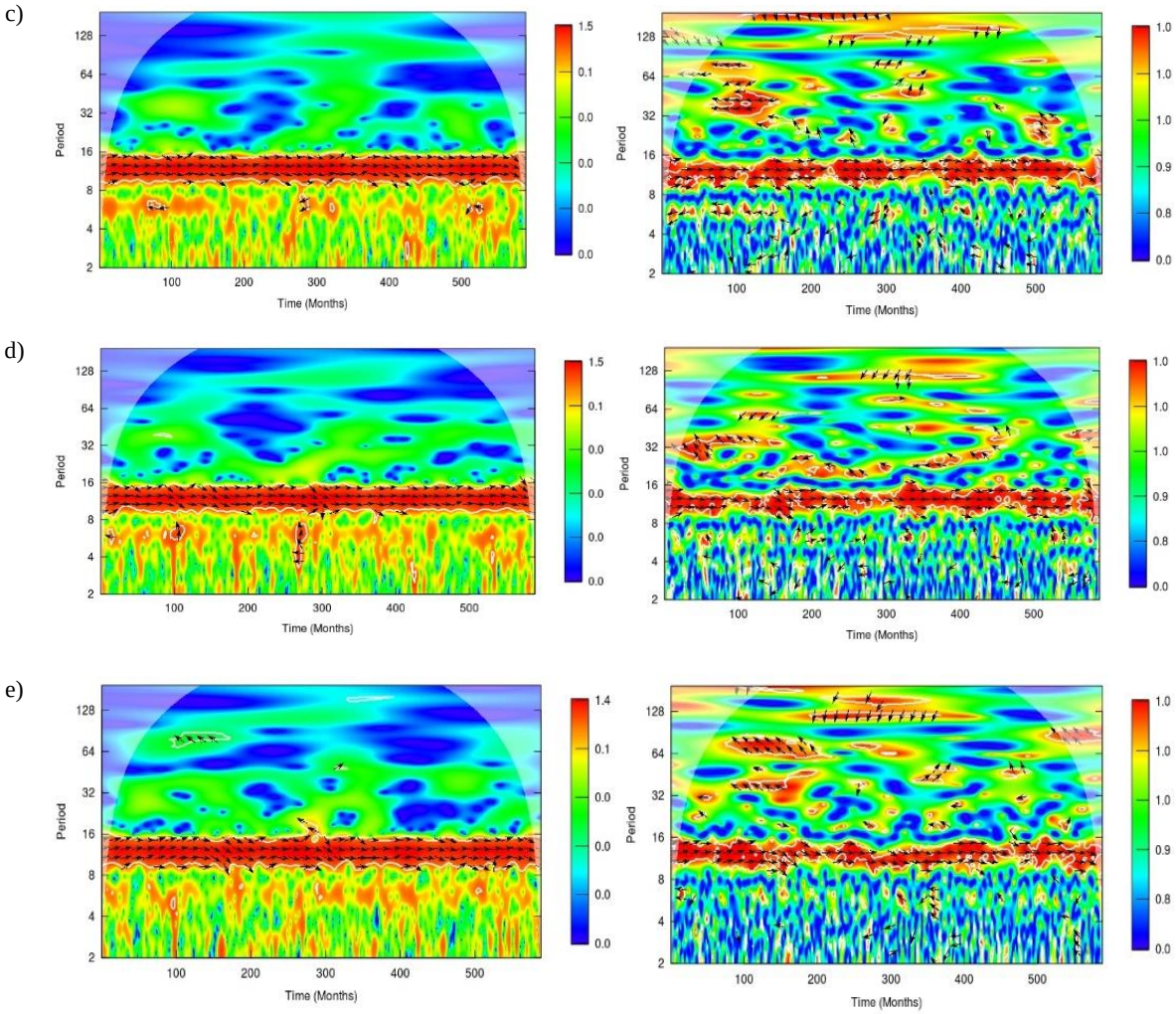

Figure 6. 9 The Cross wavelet power spectra (XWT) and wavelet coherence spectra (WCT) of rainfall with MaxT at a) CHR, b) DBR, c) GHY, d) KSH and e) TUL of NER. The cone of influence, where the edge effects might distort the picture, is designed as a lighted shadow; here, the relative phase relationship is indicated by the arrow- pointing right (left) depicting in phase (anti-phase) association.

Rainfall with MinT

As depicted by the XWT plots (Figures 6.10 a-e) all the studied locations of NER exhibited significant, strong common powers in rainfall and MinT to be in-phase also in the period band of 8-16 months. No strong powers could be seen to be anti-phase at any site (except in KSH around 100th and 260th month of observation period, i.e., around the year 1977 and 1990 in the period band of 4-8 months). However, a detailed view could be seen in the WCT plots (Figures 6.10 a-e), where inter-decadal, anti-phase association of rainfall with MinT were present in the high frequency bands (4-8 months period) in case of CHR. The other locations also exhibited intermittent anti-phase associations in the same band. On the other hand, the low frequency band of

64-128 months period displayed in phase association mostly after the 340th month of observational data (after year 1997) at CHR and KSH.

XWT WCT

a)

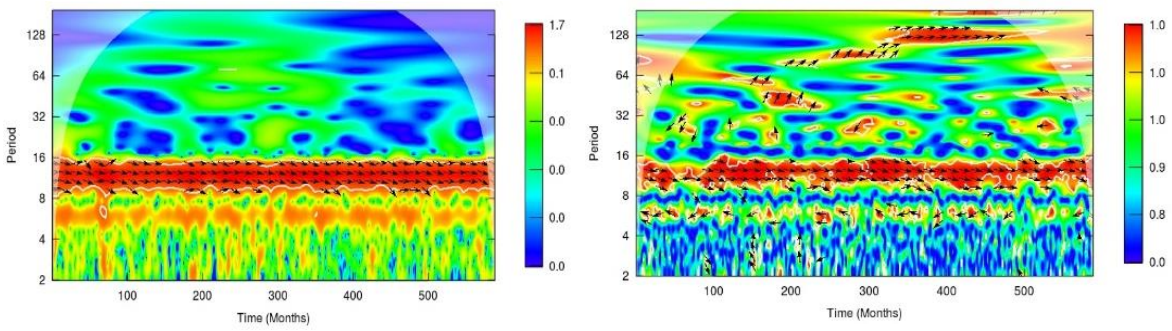

b)

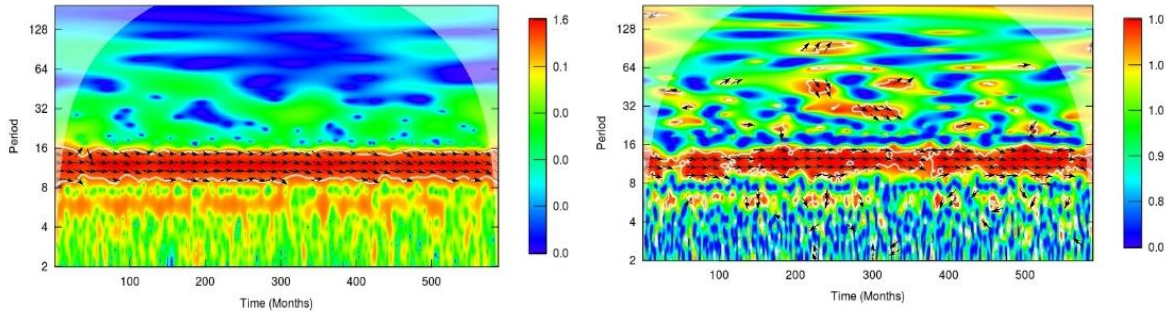

c)

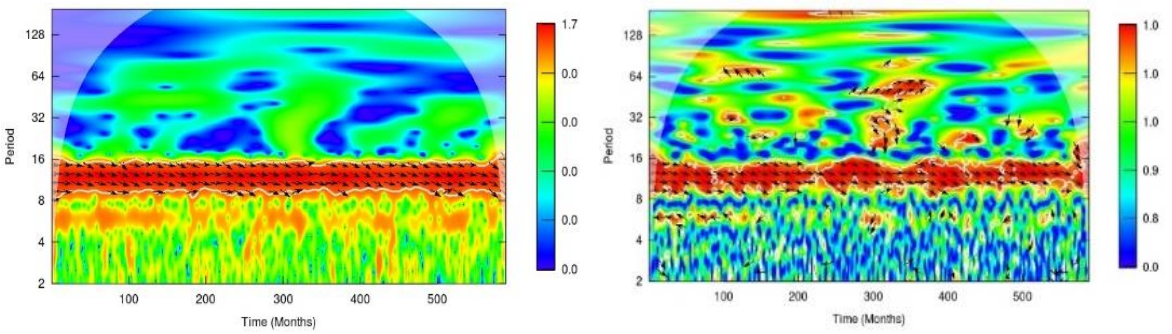

d)

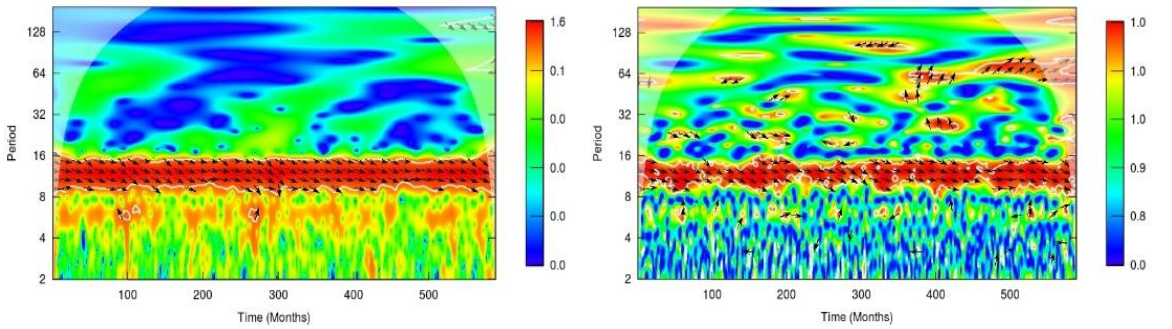

e)

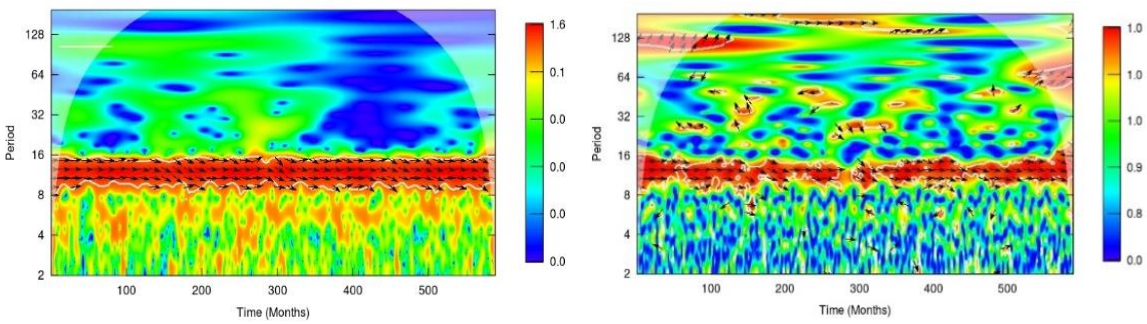

Figure 6. 10 The Cross wavelet power spectra (XWT) and wavelet coherence spectra (WCT) of rainfall and MinT at a) CHR, b) DBR, c) GHY, d) KSH and e) TUL of NER. The cone of influence, where the edge effects might distort the picture, is designed as a lighted shadow; here, the relative phase relationship is indicated by the arrow- pointing right (left) depicting in phase (anti-phase) association.

Rainfall with RH

The XWT plots (Figure 6.11 a-e) revealed significant strong common power in the 8-16 months period band between rainfall and RH like the earlier cases. The power in this band was in phase at CHR and DBR, however, the rest of the studied locations showed intermittent phase reversal. The WCT plots (Figure 6.11 a-e) revealed a detailed view where the 8-16 months period band could be seen to be present in a rugged manner at most of the locations except CHR. Among the study areas, KSH showed the most discontinuity in coherence structure here. The phase reversals were the same as in the XWT results. Significant coherence could be seen in the period band of 64-128 months at CHR from the starting to the 150th, around 250th-290th month of observation (year 1981 and 1989-1993 respectively), DBR from 340th-500th month of observation (year 1997-2010), GHY from 400th-500th month of observation (year 2002-2010), KSH between 140th-160th and around 300th month of observation (year 1980-1982 and 1994) and TUL before 210th month of observation (before year 1986).

XWT WCT

a)

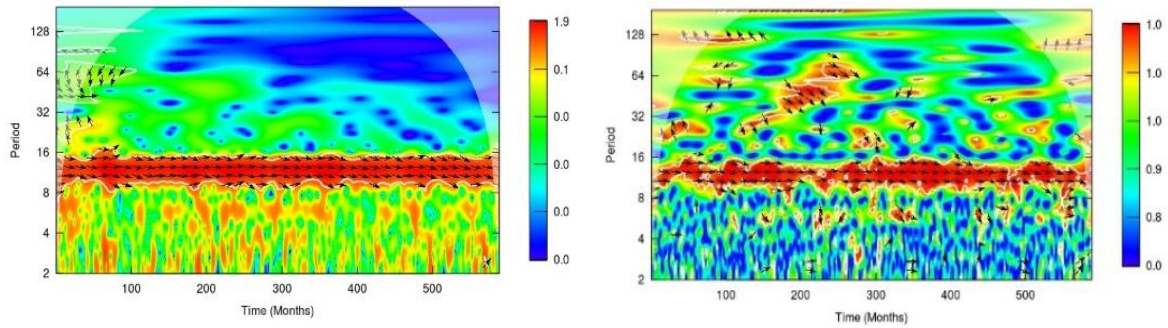
Period
Time (Months)

b)

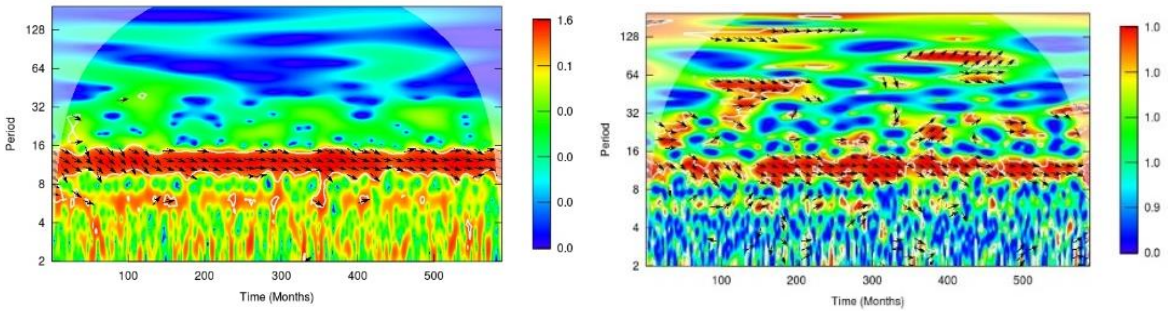
Period
Time (Months)

c)

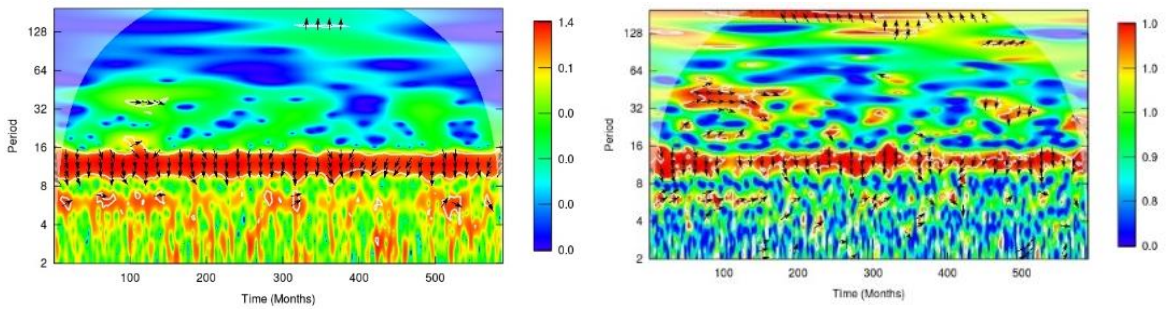
Period
Time (Months)

d)

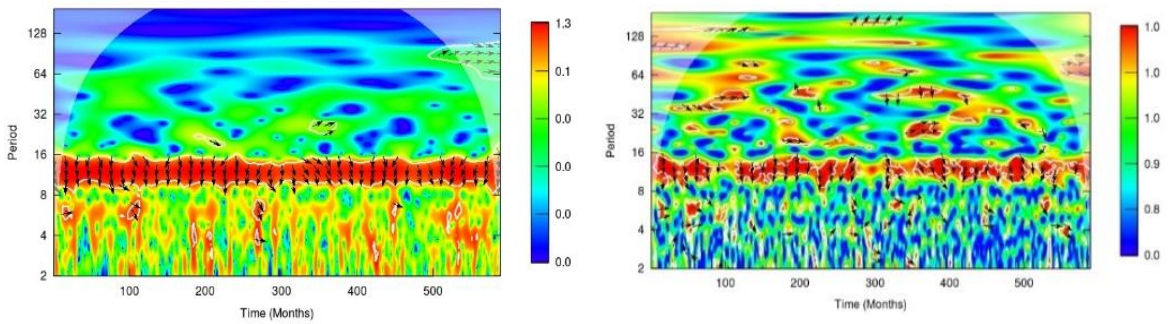
Period
Time (Months)

e)

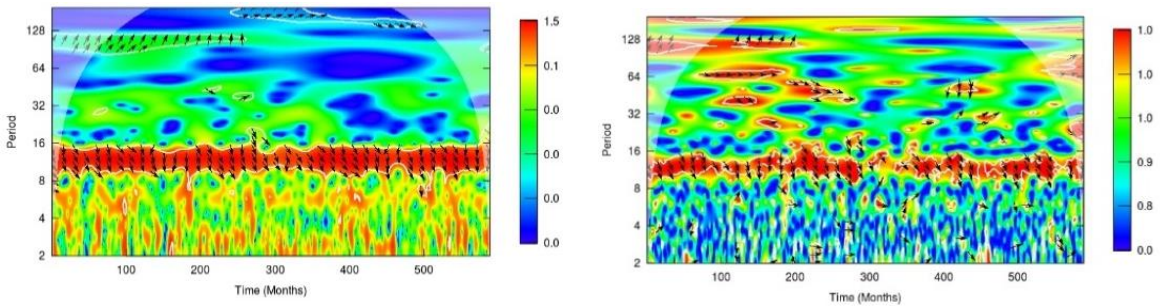

Figure 6. 11 The Cross wavelet power spectra (XWT) and wavelet coherence spectra (WCT) of rainfall with RH at a) CHR, b) DBR, c) GHY, d) KSH and e) TUL of NER. The cone of influence, where the edge effects might distort the picture, is designed as a lighted shadow; here, the relative phase relationship is indicated by the arrow- pointing right (left) depicting in phase (anti-phase) association.

Rainfall with SLP

The XWT plots between rainfall and SLP also displayed significant strong common power in the period band of 8-16 months (Figure 6.12 a-e). However, this power was anti-phase throughout the study period across all the selected locations. The WCT plots (Figure 6.12 a-e) detected strong significant coherence in this band and the phase-lock pattern was prominent. Intermittent strong, significant coherence was observed in the period band of 4-8 months also in case of CHR and DBR. WCT at CHR also revealed strong significant coherence between the 150^{th}-300^{th} month and 340^{th}-400^{th} month () in the 32-64 months period band. The later coherence structure was also seen in case of GHY and TUL in the same period band. Other than this, all the selected location of NER exhibited strong coherence in the low frequency band of 64-128 months period. After the year 1992 (after the 280^{th} month of observation period), KSH displayed another strong coherence in the low frequency band of 128^{th} month period.

XWT WCT

a)

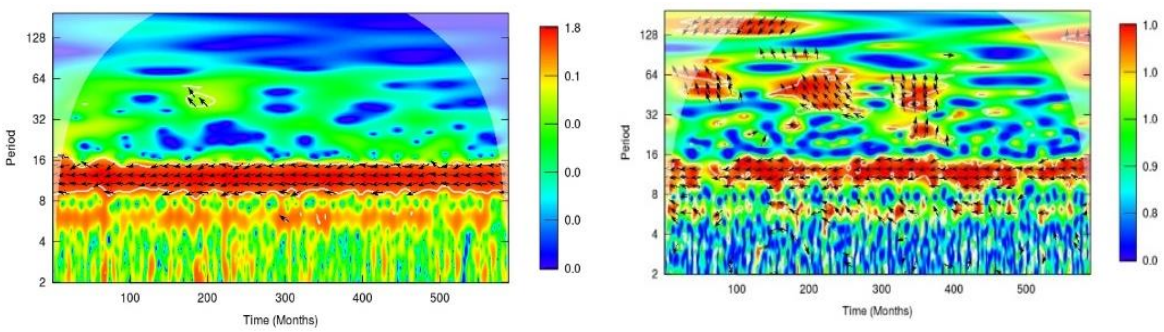
Period
Time (Months)

b)

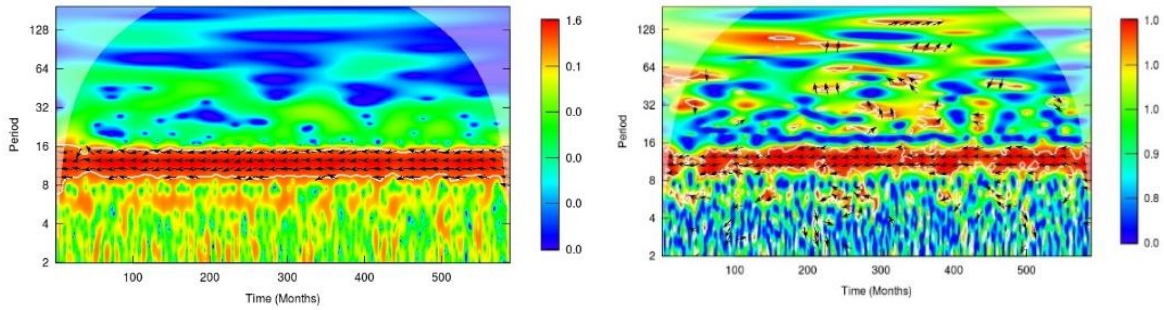
Period
Time (Months)

c)

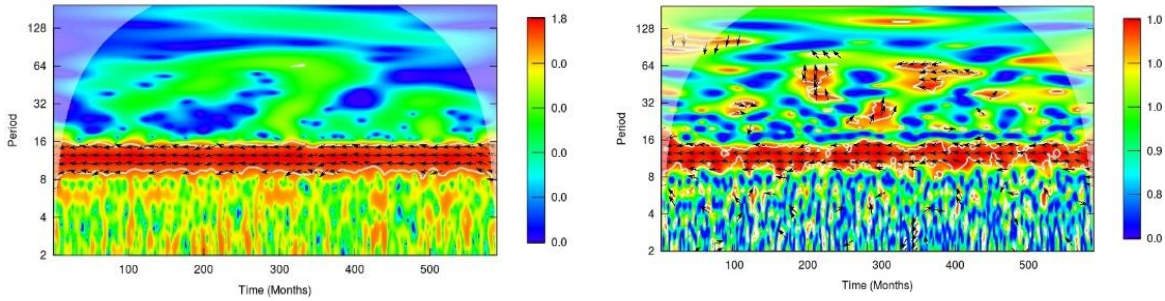
Period
Time (Months)

d)

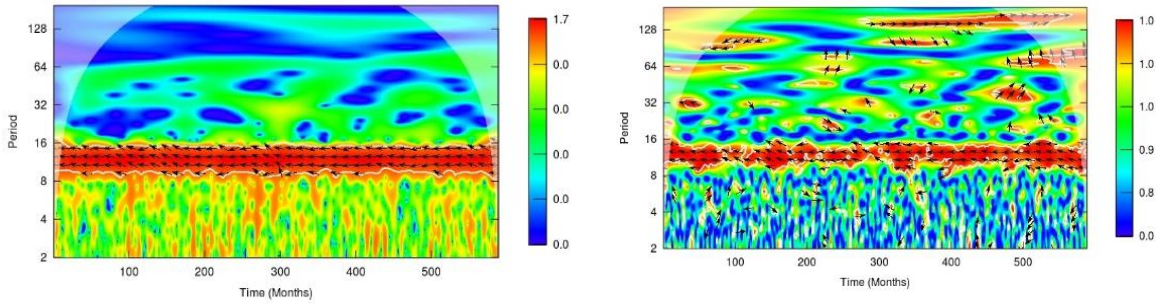
Period
Time (Months)

e)

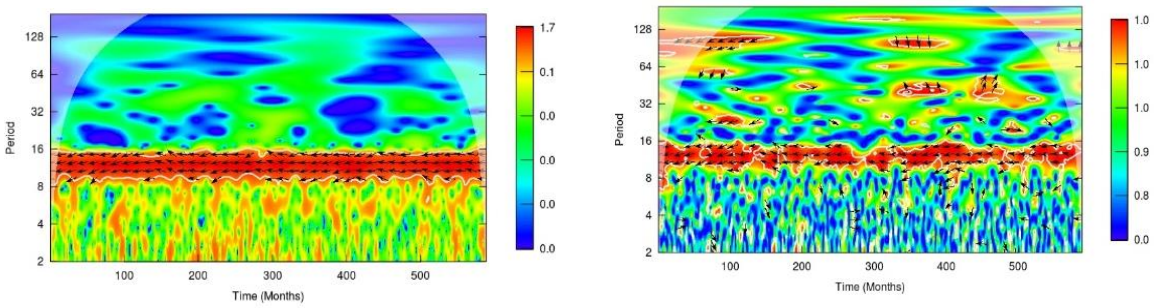

Figure 6. 12 The Cross wavelet power spectra (XWT) and wavelet coherence spectra (WCT) of rainfall with SLP at a) CHR, b) DBR, c) GHY, d) KSH and e) TUL of NER. The cone of influence, where the edge effects might distort the picture, is designed as a lighted shadow; here, the relative phase relationship is indicated by the arrow- pointing right (left) depicting in phase (anti-phase) association.

Rainfall with WS

As the observational pairs, rainfall with WS exhibited strong common powers (in phase) in the 8-12 months period band at all the studied locations of NER as evident in the XWT plots (Figure 6.13 a-e). However, the distribution of this power was discontinuous throughout the observational period at CHR and TUL. All the locations exhibited common significant power in the low frequency band too (≥128 months period band). The WCT plots (Figure 6.13 a-e) provided a detailed view. Here, the discontinuity in the coherence in 8-16 months period band could be distinctly seen with variation in phase structure. The WCT plots however, did not clearly reveal the coherence in the low frequency band (≥128 months period band). But intermittent coherence was evident in the low frequency band 16-64 months period band.

XWT WCT

a)

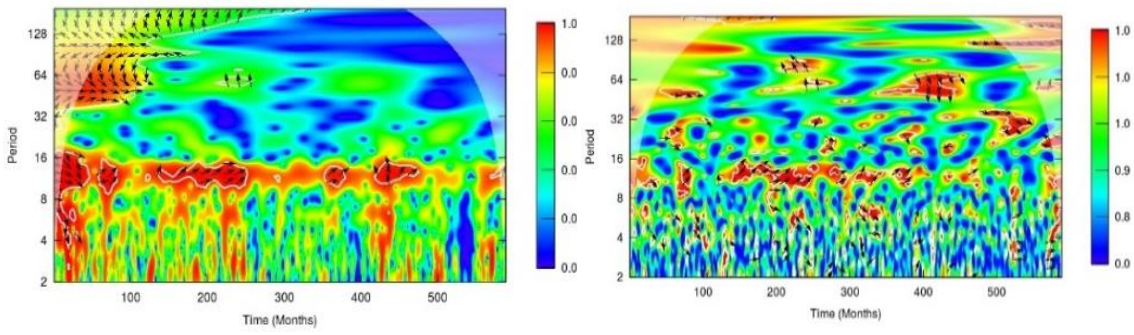

b)

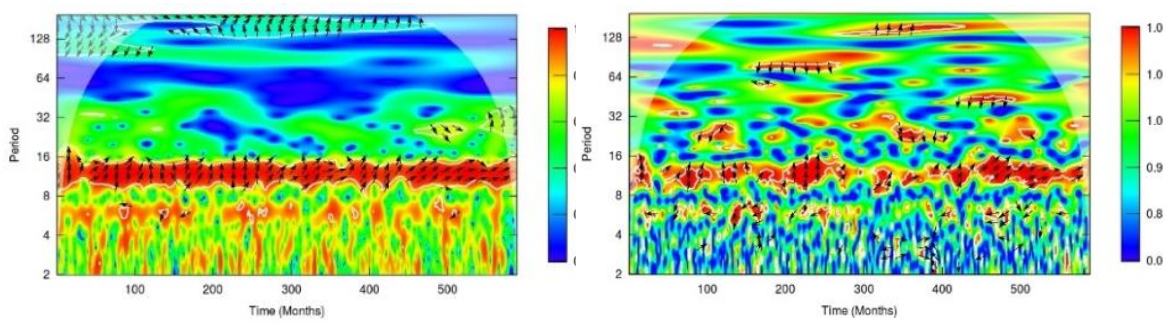

c)

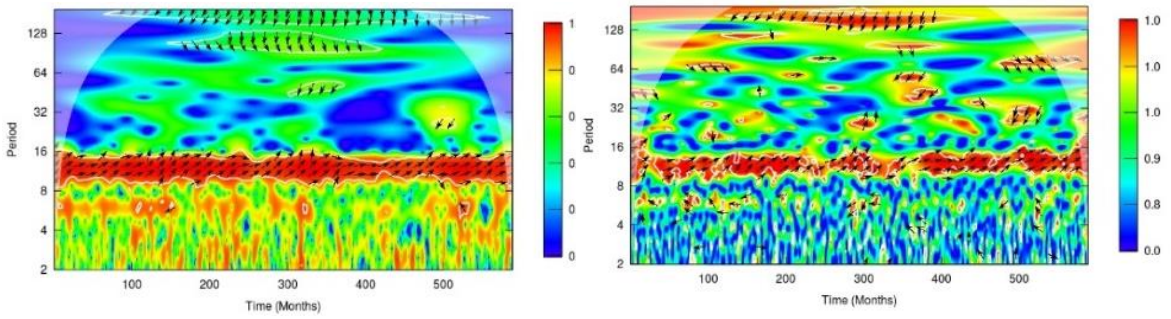

d)

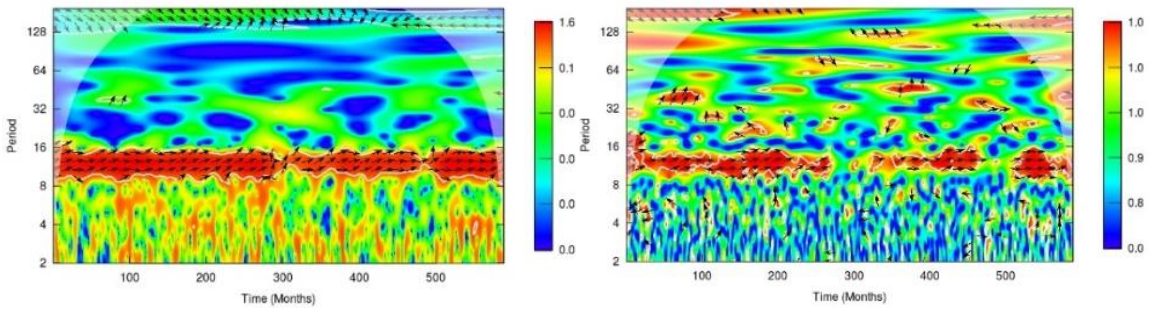

e)

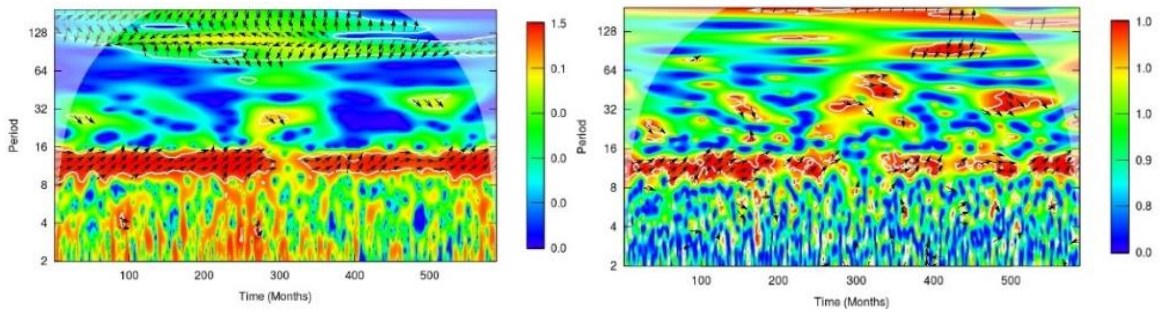

Figure 6. 13 The Cross wavelet power spectra (XWT) and wavelet coherence spectra (WCT) of rainfall with WS at a) CHR, b) DBR, c) GHY, d) KSH and e) TUL of NER. The cone of influence, where the edge effects might distort the picture, is designed as a lighted shadow; here, the relative phase relationship is indicated by the arrow- pointing right (left) depicting in phase (anti-phase) association.

6.4 Summary

SSA and wavelet tools are recognized as an effective tool in identification and isolation of dominant features present in a time series and are widely used in the field of climate science for their efficiency in use. Wavelet is a relatively newer technique than SSA, which explores the characteristics of a time series or the commonalities in the features of two time series in both time-frequency domain, while SSA only operates in time domain. In this regard, we applied both of these tools in identifying the contributing components of a series and their variable contribution by deconstruction and reconstruction. In this study, we've analyzed the rainfall series separately, to look for the characteristic structures constituting each one of them over different selected locations of NER, as well as the contribution of these features to the rainfall series using SSA. It was found that, the major contribution to a series (about >45%) comes from the trend component, followed by a periodic component of 12 months over NER. Another periodic component of 6 months was also prominent in all the studied locations, while periodicities of 4 and 2.4 months were also noticed in some of the locations. It was noticeable that in some of the cases more than two trend components were also present.

Wavelet analyses covered the purpose of determining the locations of the possible periodic components in individual rainfall series in both time and frequency domain. In all of the rainfall series detection of significant periodic components were noticed to be existing in the 8-16 months period band. A ridge in the 12 months period of the wavelet spectra confirmed the findings from chapter 4 as well as from SSA analyses. Commonality was found in the higher power of this 8-16 months period band between rainfall and different meteorological variables of interest across all sites. Significant strong association of rainfall with MaxT, MinT, RH, SLP and WS was also evident in this period band as per the results obtained from wavelet coherence analyses. Apart from this period band, both high and low frequency bands (2-8 months period bands and 64-128 months period bands respectively) displayed inter-relationship between rainfall and selected variables at some locations. Intermittent strong association of rainfall with other variables were also evident in some cases. As evident from the wavelet analyses, inter-decadal associations were also detected in some period bands at certain locations. Among these explored associations, the strong significant association that was present in the 8-12 months period band was in phase (usually the

second variable was leading) with almost all the variables except SLP. Anti-phase associations were mostly distinct in the low frequency bands, while in the high frequency bands most of the associations were in phase. Significant phase reversal of 180^o was also evident in some cases. Significant inter-relations could be seen in the association of rainfall with most of the variables, after 1997 or between the year 1997-2010. In case of the intermittent coherence, rainfall displayed significant association with the other meteorological variables near the year 1977 and 1992 in some of the studied locations. Thus, by exploring the meteorological time series with these two tools, we could see probable induced changes occurring after certain time frame leading into existence of repeating patterns at localized portions of the time series in time-frequency scale. The inter-associations of rainfall and other meteorological variables in multi-resolution had been dealt in the next chapter (Chapter 7).

In this section prediction of characteristic feature in the rainfall series are not included. Future works may include the scope of extracting the trends and forecasting the trends in an increasing climate scenario.

6.5 References

[1] Golyandina N. and Korobeynikov, A. Basic Singular Spectrum Analysis and forecasting with R. *Computational Sattostics and Data Analysis*, 71:934-954, 2014. DOI: 10.1016/j.csda.2013.04.009.

[2] Broomhead, D.S. and King, G.P. Extracting qualitative dynamics from experimental data. *Physica*, 20D:217-236, 1986. DOI: :10.1016/0167-2789(86)90031-X.

[3] Vautard, R. and Ghil, M. Singular-spectrum analysis in nonlinear dynamics, with applications to paleoclimatic time series. *Physica D*, 35:395-424, 1989. DOI: https://doi.org/10.1016/0167-2789(89)90077-8.

[4] Deng, C. Time Series Decomposition Using Singular Spectrum Analysis. Master's Thesis, Department of Mathematics East Tennessee State University, Electronic Theses and Dissertations. Paper 2352, 2014.

[5] Golyandina N. Particularities and commonalities of singular spectrum analysis as a method of time series analysis and signal processing. *Computational Statistics*, 1487:1-39, 2020.

[6] Hassani, H. Singular Spectrum Analysis: Methodology and Comparison. *Journal of Data Science*, 5:239-257, 2007.

[7] Garcia, J. A., Serrano, A. and de la Cruz Gallego, M. A spectral analysis of Iberian Peninsula monthly rainfall. *Theoretical and Applied Climatology*, 71:77-95, 2002.

[8] Hassani, H. and Thomakos, D. A review on singular spectrum analysis for economic and financial time series. *Statistics and Its Interfere*, 3:377-397, 2010.

[9] Marques, C.A.F., Ferreira, J.A., Rocha, A., Castanheira, J.M., Melo-Goncalves, P., Vaz, N. and Dias, J.M. Singular spectrum analysis and forecasting of hydrological time series. *Physics and Chemistry of the Earth*, 31:1172-1179, 2006.

[10] Álvarez-Meza, A.M., Acosta-Medina, C.D. and Castellanos-Dom´ınguez, G. Automatic Singular Spectrum Analysis for Time-Series Decomposition. In *ESANN 2013 proceedings*, European Symposium on Artificial Neural Networks, Computational Intelligence and Machine Learning, 2013.

[11] Shaharudin, S.M., Ahmad, N. and Zainuddin, N.H. Modified singular spectrum analysis in identifying rainfall trend over peninsular Malaysia. Indonesian Journal of Electrical *Engineering and Computer Science*, 15(1):283-293, 2019.

[12] Unnikrishnan, P., Jothiprakash, V. *Journal of Hydrological Engineering*, 27(9): 06022001-1- 06022001-6, 2022.

[13] Rangarajan, G.K. Singular spectral analysis of homogeneous Indian Monsoon (HIM) rainfall. *Proc. Indian Acad. Sci. (Earth Planet. Sci.)*, 103(4):439-448, 1994.

[14] Unnikrishnan, P., Jothiprakash, V. Extraction of Nonlinear Rainfall trends Using Singular Spectrum Analysis. *Journal of Hydrological Engineering*, 20(12): 05015007-1- 05015007-15, 2015.

[15] Aswathaiah1, U. and Nandagiri, L. Extraction of Nonlinear Trends in Time Series of Rainfall Using Singular Spectrum Analysis. *Journal of Hydrological Engineering*, 25(12): 04020053-1- 04020053-16, 2020.

[16] Baratta, D., Cicioni, G., Masulli, F. and Studer, L. Application of an ensemble technique based on singular spectrum analysis to daily rainfall forecasting. *Neural Networks*, 16:375-387, 2003.

[17] Pham, Q.B., Yang, Tao-Chang, Kuo, Chen-Min and Tseng, Hung-Wei. Coupling Singular Spectrum Analysis with Least Square Support Vector Machine to Improve Accuracy of SPI Drought Forecasting. *Water Resources Management*, 35:847–868, 2021.

[18] Reddy, P.C.S., Sucharitha, Y. And Narayana, G.S. Development of rainfall forecasting model using machine learning with singular spectrum analysis. *IIUM Engineering Journal*, 23(1):172-186, 2022.

[19] Amara, G. An introduction to wavelets. *IEEE Computational Science and Engineering*, 2:50-61, 1995. DOI: 10.1109/99.388960.

[20] Das, J., Jha, S. and Goyal, M. On the relationship of climatic and monsoon teleconnections with monthly precipitation over meteorologically homogenous regions in India: Wavelet & global coherence approaches. *Atmospheric Research*, 238:1-12, 2020.

[21] Kwon, Hyun-Han, Lall, U. and Khalil, A.F. Stochastic simulation model for nonstationary time series using an autoregressive wavelet decomposition: Applications to rainfall and temperature. *Water Resources Research*, 43(W05407)1-15, 2007.

[22] Partal, T. and Küçük, M. Long-term trend analysis using discrete wavelet components of annual precipitations measurements in Marmara region (Turkey). *Physics and Chemistry of the Earth*, 31:1189-1200, 2006.

[23] Marković D. and Koch, M. Wavelet and scaling analysis of monthly precipitation extremes in Germany in the 20th century: Interannual to interdecadal oscillations and the North Atlantic Oscillation influence. *Water Resources Research*, 41(W09420):1-13, 2005. DOI: 10.1029/2004WR003843

[24] Liu, H., Tian, Hong-qi, Pan, Di-fu and Li, Yan-fei. Forecasting models for wind speed using wavelet, wavelet packet, time series and Artificial Neural Networks, *Applied Energy*, 107:191-208, 2013.

[25] Kang, D. and Wang, H. Analysis on the decadal scale variation of the dust storm in North China. *Science in China Earth Sciences*, 48(12):2260—2266, 2005.

[26] Li, J., Pu, J., Zhang, T., Wang, S., Huo, W. and Yuan, D. Investigation of transport properties and characteristics of a large karst aquifer system in southern

China using correlation, spectral, and wavelet analyses. *Environmental Earth Sciences*, 80:84, 2021. DOI: https://doi.org/10.1007/s12665-020-09366-9.

[27] Moghram, I. and Saifur, R. Analysis and evaluation of five short-term load forecasting techniques. *Proceedings of the IEEE Transactions on Power Systems*, 4(4):1484-1491, 1989.

[28] Aussem, A., Campbell, J. and Murtagh, F. Wavelet-based feature extraction and decomposition strategies for financial forecasting. *International Journal of Computational Intelligence in finance*, 6:5-12, 1998.

[29] Khotanzad, A., Afkhami-Rohani, R., Lu, T.L., Abaye, A., Davis, M. and Maratukulam, D.J. ANNSTLF- A neural-network based electric load forecasting system. *IEEE Transactions on Neural Networks*, 8(4), 1997.

[30] Torrence, C. and Compo, G.P. A Practical Guide to Wavelet Analysis. *Bulletin of the American Meteorological Society*, 79(1):61-78, 1998.

[31] Kestin, T.S., Karoly, D.J. and Yano, Jun-Ichi. Time–Frequency Variability of ENSO and Stochastic Simulations. *Journal of Climate,* 11:2258-2272, 1998.

[32] Nakken, M. Wavelet analysis of rainfall–runoff variability isolating climatic from anthropogenic patterns. *Environmental Modelling & Software*, 14:283–295, 1999.

[33] Torrence, C. and Webster, P.J. Interdecadal Changes in the ENSO–Monsoon System, *Journal of Climate*, 12:2679-2690, 1999.

[34] Narasimha, R. and Bhattacharyya, S. A wavelet cross-spectral analysis of solar–ENSO–rainfall connections in the Indian monsoons. *Applied and Computational Harmonic Analysis*, 28:285-295, 2010.

[35] Subash, N., Sikka, A.K. and Mohan, H.S.R. An investigation into observational characteristics of rainfall and temperature in Central Northeast India—a historical perspective 1889–2008. *Theoretical and Applied Climatology*, 103:305-319, 2011. DOI: 10.1007/s00704-010-0299-2.

[36] Rathinasamy, M., Agarwal, A., Sivakumart, B., Marwan, N. and Kurths, J. Wavelet analysis of precipitation extremes over India and teleconnections to climate indices. Stochastic *Environmental Research and Risk Assessment*, 33:2053–2069, 2019. DOI: https://doi.org/10.1007/s00477-019-01738-3

[37] Elsner, J.B., Tsonis, A.A. Singular spectrum analysis: A new tool in time series analysis. *Plenum Press*, New York, and London, 1996. DOI: https://doi.org/10.1038/353551a0.

[38] Golyandina, N., Nekrutkin, V. and Zhiglijavsky, A. Analysis of time series structure- SSA and related techniques. *Chapman and Hall/CRC*, 2001.

[39] Ruelle, D. Large volume limit of the distribution of exponents in turbulence. *Communications in Mathematical Physics*, 87:287, 1980. DOI: https://doi.org/10.1007/BF01218566.

[40] Takens, F. Detecting strange attractors in turbulence. In *Lecture Notes in Mathematics, Dynamical Systems and Turbulence,* edited by D.A. Rand and L.S. Young, Springer-Verlag, New York, volume 898, pages 66-381, 1981. DOI: https://doi.org/10.1007/BFb0091924.

[41] Kumar, U. A modelling study of ozone concentration in ambient urban environment. *Thesis submitted to the Jawaharlal Nehru University*, 2006.

[42] Vautard, R., Yiou, P. and Ghil, M. Singular spectrum analysis: A tool kit for short, noisy chaotic signals. *Physica D*, 58:95-126, 1992. DOI: https://doi.org/10.1016/0167-2789(92)90103-T.

[43] Plaut, G., and Vautard, R. Spells of low frequency oscillations and weather regimes in the northern hemispheres. *Journal of Atmospheric Sciences*, 51:210-236, 1994.

[44] Press, W.H., Teukolsky, S.A., Vellerling, W.T. and Flannery, B.P. Numerical recipes in C: The art of scientific computing. *Cambridge University Press, Cambridge*, 1992.

[45] Yiou, P., Ghil, M., Jouzel, J., Paillard, D. and Vautard, R. Non-linear variability of the climate system from singular and power spectra of quaternary records. *Climate dynamics*, 9:37, 1994. DOI: https://doi.org/10.1007/BF00207933.

[46] Rasmussom, E.M., Wang, X. and Ropelewski, C.F. The biennial component of ENSO variability. *Journal of Marine Systems*, 1:71-96, 1990. DOI: https://doi.org/10.1016/0924-7963(90)90153-2.

[47] Walker, J.S. A primer on wavelets and their scientific applications. *Chapman & Hall/CRC*, USA, 1999.

[48] Percival, D.B. and Walden, A.T. Wavelet methods for time series analysis. *Cambridge University Press, U.K.*, 2000.

[49] Tran, V. G., Grieu, S., Polit, M., Tran, Q. T. and Tran, H. L. Forecasting of wind speed using wavelets analysis and cascade-correlation neural networks. In *European Wind Energy Conference and Exhibition (EWEC)*, Marseille: France, (2009), 2010.

[50] Grinsted, A., Moore, J.C. and Javrejeva, S. Application of the cross wavelet transform and wavelet coherence to geophysical time series. *Nonlinear Processes in Geophysics, 11:561*-566, 2004.

[51] Golyandina, N. and Korobeynikov, A. Basic Singular Spectrum Analysis and forecasting with R. *Computational Statistics and Data Analysis*, 71:934-954, 2014.